ELSEVIER

NeuroImage

www.elsevier.com/locate/ynimg
NeuroImage 40 (2008) 26–34

# Robust estimation of the arterial input function for Logan plots using an intersectional searching algorithm and clustering in positron emission tomography for neuroreceptor imaging

Mika Naganawa,[a,b] Yuichi Kimura,[a,*] Junichi Yano,[c] Masahiro Mishina,[d] Masao Yanagisawa,[c] Kenji Ishii,[e] Keiichi Oda,[e] and Kiichi Ishiwata[e]

[a]*Molecular Imaging Center, National Institute of Radiological Sciences, 4-9-1, Anagawa, Inage, Chiba-shi, Chiba, 263-8555, Japan*
[b]*Yale PET Center, School of Medicine, Yale University, New Haven, CT, USA*
[c]*Graduate School of Science and Engineering, Waseda University, Tokyo, Japan*
[d]*Neurological Institute, Nippon Medical School Chiba-Hokusoh Hospital, Chiba, Japan*
[e]*Positron Medical Center, Tokyo Metropolitan Institute of Gerontology, Tokyo, Japan*

Received 9 June 2007; revised 22 October 2007; accepted 17 November 2007
Available online 4 December 2007

**The Logan plot is a powerful algorithm used to generate binding-potential images from dynamic positron emission tomography (PET) images in neuroreceptor studies. However, it requires arterial blood sampling and metabolite correction to provide an input function, and clinically it is preferable that this need for arterial blood sampling be obviated. Estimation of the input function with metabolite correction using an intersectional searching algorithm (ISA) has been proposed. The ISA seeks the input function from the intersection between the planes spanned by measured radioactivity curves in tissue and their cumulative integrals in data space. However, the ISA is sensitive to noise included in measured curves, and it often fails to estimate the input function. In this paper, we propose a robust estimation of the cumulative integral of the plasma time–activity curve (pTAC) using ISA (robust EPISA) to overcome noise issues. The EPISA reduces noise in the measured PET data using averaging and clustering that gathers radioactivity curves with similar kinetic parameters. We confirmed that a little noise made the estimation of the input function extremely difficult in the simulation. The robust EPISA was validated by application to eight real dynamic [$^{11}$C]TMSX PET data sets used to visualize adenosine $A_{2A}$ receptors and four real dynamic [$^{11}$C]PIB PET data sets used to visualize amyloid-beta plaque. Peripherally, the latter showed faster metabolism than the former. The clustering operation improved the signal-to-noise ratio for the PET data sufficiently to estimate the input function, and the calculated neuroreceptor images had a quality equivalent to that using measured pTACs after metabolite correction. Our proposed method noninvasively yields an alternative input function for Logan plots, allowing the Logan plot to be more useful in neuroreceptor studies.**


*Keywords:* Positron emission tomography; Clustering; Intersectional searching algorithm; Arterial blood sampling; Logan plot

## Introduction

The Logan plot (Logan et al., 1990) is a graphical approach that estimates volume of distribution ($V_T$) from the slope of a plot. $V_T$ refers to the sum of the volume of distributions in the free, nonspecific binding, and specific binding compartments (Koeppe et al., 1991; Innis et al., 2007). Because this algorithm achieves more robust and faster estimation compared with nonlinear least squares methods (Carson, 2002), it is widely used for generating parametric images of $V_T$ in neuroreceptor mapping. The Logan plot requires two measurable data sets: one is obtained by dynamic PET scanning, and the other is obtained by serial arterial blood sampling. If the serial arterial blood sampling can be omitted, the Logan plot becomes a more useful and easy-to-use approach. There are several approaches to avoiding invasive arterial blood sampling. Reference-region-based Logan plot (Logan et al., 1996) cancels out the term of the integral of the plasma time–activity curve (pTAC) using a tissue time–activity curve (tTAC) in reference regions where the target receptor is negligible. Although the term relating to the pTAC is expelled, the estimation equation still includes an efflux parameter, $k_2$ [1/min]. It is sometimes difficult to know the value of $k_2$ about reference regions in advance. If an equilibrium state is achieved between tTAC and pTAC, a priori knowledge of $k_2$ is not necessary, but such a

* Corresponding author.
*E-mail address:* ukimura@ieee.org (Y. Kimura).
**Available online on ScienceDirect (www.sciencedirect.com).**

1053-8119/$ - see front matter © 2007 Elsevier Inc. All rights reserved.
doi:10.1016/j.neuroimage.2007.11.035

situation is not always realized. Another approach, which we have previously proposed, is based on a statistical model: independent component analysis (Naganawa et al., 2005a,b) and variational Bayes (Naganawa et al., 2007a). These methods assume a factor analysis model in which each voxel includes the radioactivities from tissue and blood, and estimates the time–activity curve (TAC) of whole blood radioactivity. The estimated blood curve was successfully used in Logan plots as an alternative to the measured pTAC. Note that the plasma-to-whole blood ratio should be constant in the time for which the Logan plot was applied (Naganawa et al., 2005b), and the estimated blood curve includes the radioactivity in metabolites.

In applying the Logan plot, an input blood function appears in a form of the cumulative integral of the pTAC (intpTAC). It is desirable for the intpTAC to be corrected metabolically. Wang et al. proposed an intersectional searching algorithm (ISA) to estimate the intpTAC directly (Wang et al., 2005). The metabolite-corrected intpTAC will be theoretically obtained using their algorithm. However, one aspect to be considered is noise in the measured tTACs. Because of its mathematical nature, the ISA is very sensitive to noise, and it is thus important to reduce the noise effectively in estimating intpTAC. We have developed methods to reduce the measurement noise using clustering based on each TAC's kinetics (Kimura et al., 1999, 2005a,b). It is expected that our clustering method will improve estimation using ISA. In this paper, we propose a method for robust extraction of the intpTAC using ISA and clustering (robust EPISA). We clarify the sensitivity of the ISA to the measurement noise using simulations, and we investigate the applicability of the robust EPISA by applying it to dynamic PET data using [7-methyl-$^{11}$C]-(*E*)-8-(3,4,5-trimethoxystyryl)-1,3,7-trimethylxanthine ([$^{11}$C]TMSX), which visualizes adenosine $A_{2A}$ receptors (Ishiwata et al., 2000, 2005; Mishina et al., 2007), and [*N*-methyl-$^{11}$C]2-(4′-methylaminophenyl)-6-hydroxy-benzothiazole] ([$^{11}$C]PIB), which visualizes amyloid-beta plaque (Mathis et al., 2003; Klunk et al., 2004).

## Theory

### *ISA*

ISA (Wang et al., 2005) estimates the intpTAC using at least two tTACs with mutually different shapes and the corresponding cumulative integral of the tTACs (inttTAC) based on the equations for the Logan plot. This section provides an overview of the ISA and discusses its drawbacks. The equation for the Logan plot is described as

$$\frac{\int_0^T c^{(i)}(t)\mathrm{d}t}{c^{(i)}(T)} = d^{(i)}\frac{\int_0^T c_p(t)\mathrm{d}t}{c^{(i)}(T)} + b^{(i)}, \tag{1}$$

where $c^{(i)}(t)$ is a tTAC at the $i$th voxel or region and $c_p(t)$ is a pTAC. $\int_0^T c^{(i)}(t)\mathrm{d}t$ and $\int_0^T c_p(t)\mathrm{d}t$ are inttTAC at the $i$th voxel and intpTAC, respectively. For time $T \geq t^*$, the second term $b^{(i)}$ ($<0$) is a constant, and $d^{(i)}$ corresponds to a $V_T$. Eq. (1) is arranged for $\int_0^T c_p(t)\mathrm{d}t$ as

$$\begin{aligned}\int_0^T c_p(t)\mathrm{d}t &= \frac{-b^{(i)}}{d^{(i)}}c^{(i)}(T) + \frac{1}{d^{(i)}}\int_0^T c^{(i)}(t)\mathrm{d}t \\ &= a_1^{(i)}c^{(i)}(T) + a_2^{(i)}\int_0^T c^{(i)}(t)\mathrm{d}t.\end{aligned} \tag{2}$$

Because the values of $d^{(i)}$ and $b^{(i)}$ are constant, constant coefficients $b^{(i)}/d^{(i)}$ and $1/d^{(i)}$ are denoted as $a_1^{(i)}$ and $a_2^{(i)}$, respectively. Assuming that a tTAC is measured at times $T=t_1, t_2, \ldots, t_m$, Eq. (2) can be written in terms of vectors as

$$\boldsymbol{c}_{\mathrm{pint}} = a_1^{(i)}\boldsymbol{c}^{(i)} + a_2^{(i)}\boldsymbol{c}_{\mathrm{int}}^{(i)}, \tag{3}$$

where $\boldsymbol{c}_{\mathrm{pint}}$, $\boldsymbol{c}^{(i)}$, and $\boldsymbol{c}_{\mathrm{int}}^{(i)}$ are column vectors of $m$ elements corresponding to $\int_0^T c_p(t)\mathrm{d}t$, $c^{(i)}(T)$, and $\int_0^T c^{(i)}(t)\mathrm{d}t$, respectively. Because $\boldsymbol{c}_{\mathrm{pint}}$ is a common vector between the $i$th and $j$th voxels or regions ($i \neq j$), the following equation is obtained.

$$a_1^{(i)}\boldsymbol{c}^{(i)} + a_2^{(i)}\boldsymbol{c}_{\mathrm{int}}^{(i)} = a_1^{(j)}\boldsymbol{c}^{(j)} + a_2^{(j)}\boldsymbol{c}_{\mathrm{int}}^{(j)} \tag{4}$$

Eq. (4) can be rewritten as

$$\left(\boldsymbol{c}^{(i)}\boldsymbol{c}_{\mathrm{int}}^{(i)}\boldsymbol{c}^{(j)}\boldsymbol{c}_{\mathrm{int}}^{(j)}\right)\begin{pmatrix} a_1^{(i)} \\ a_2^{(i)} \\ -a_1^{(j)} \\ -a_2^{(j)}\end{pmatrix} = \boldsymbol{C}\boldsymbol{a} = 0. \tag{5}$$

where $\boldsymbol{C} \in \mathcal{R}^{m\times 4}$ is a matrix ($m>4$) and $\boldsymbol{a} \in \mathcal{R}^{4\times 1}$ is a column vector. Because the rank of the matrix $\boldsymbol{C}$ is at most three, the vector $\boldsymbol{a}$ can be estimated as a right singular vector corresponding to the smallest right singular value of $\boldsymbol{C}$. Because any vector whose direction is equal to the right singular vector $\boldsymbol{a}$ satisfies Eq. (5), the length of $\boldsymbol{a}$ cannot be determined. Accordingly, the absolute value of the intpTAC cannot be determined. ISA infers only the shape of the intpTAC during the period in which the Logan plot can be applied. Although the absolute value of the $V_T$ at each voxel cannot be determined using the Logan plot with ISA-estimated intpTAC, the ratio between them can be estimated. Note that the estimation of the intpTAC is limited to the range of time used for the Logan plot, because ISA is defined only on the frames where the Logan plot is applicable. Thus, ISA is useless in estimating the intpTAC at early times, and the estimated intpTAC cannot be used as an input function for the nonlinear least squares method.

Let us give a geometrical interpretation of ISA algorithm to allow intuitive understanding of the effect of noise. Eq. (3) means that the intpTAC vector $\boldsymbol{c}_{\mathrm{pint}}$ is on the plane that is spanned by the tTAC vector $\boldsymbol{c}^{(i)}$ and the inttTAC vector $\boldsymbol{c}_{\mathrm{int}}^{(i)}$. Eq. (4) shows that $\boldsymbol{c}_{\mathrm{pint}}$ is an intersectional vector of two planes by the $i$ and $j$th voxel. Fig. 1 shows the geometric relationship between intpTAC, the tTACs and the inttTACs. In reality, there is a large amount of noise in the measured PET data. Therefore, the plane spanned by the tTAC vector and the inttTAC vector is deviated from the true plane. Accordingly, the measurement noise produces estimation error in the direction of the intersectional vector $\boldsymbol{c}_{\mathrm{pint}}$.

### *Robust EPISA*

The proposed method, robust EPISA, improves the signal-to-noise ratio of the measured PET data using averaging and clustering. The voxels that locate close to each other tend to have similar kinetics. In addition, there exist tTACs that have similar kinetics but locate at separate positions. In robust EPISA, first, a spatial averaging filter is applied. Clustering is subsequently performed to gather tTACs based on their kinetics, and tTACs classified into the same cluster are averaged. Finally,

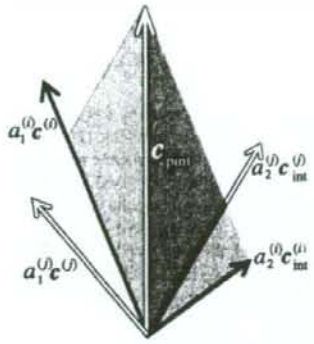


Fig. 1. Schematic illustration of a relationship between intpTAC, the tTACs, and the inttTACs. The intpTAC is estimated as an intersection vector of two planes.

the intersection-searching algorithm is applied to noise-reduced data.

To reduce noise, clustering was performed using a quantity proposed in (Kimura et al., 1999, 2002). The quantity, $R$, is defined as

$$R \equiv \frac{\int_0^T c^{(i)}(t)\mathrm{d}t}{\int_0^T tc^{(i)}(t)\mathrm{d}t} \tag{6}$$

where $T$ is the time of the final frame. The amplitude of $R$ is determined by only the shape of the tTAC emphasized by $t$. The quantity $R$ is invariant when the tTAC becomes the product of a constant $\alpha$ times the tTAC $c^{(i)}(t)$, because $\alpha$ is canceled out between the numerator and the denominator in Eq. (6). Therefore, the quantity $R$ evaluates the tTAC's shape. For example, the quantity $R$ becomes a function of a kinetic efflux parameter $k_2$ when a kinetic of the administered radioligand is described by a one-tissue two-compartment model (Kimura et al., 1999).

The actual procedures in robust EPISA are shown below.

1. The region outside the brain was excluded and voxel-based PET data were spatially averaged.
2. The quantity, $R$, was calculated about each voxel, and voxels with similar $R$ were categorized into one cluster. The same number of voxels were assigned to each cluster.
3. The tTACs categorized into the same cluster were averaged. Note that each tTAC was normalized by each time integral.
4. The intpTACs were estimated from all possible pairs of the averaged tTACs.
5. The candidate intpTACs were obtained from all estimated intpTACs by excluding failed curves, and the final result was the averaged candidate intpTACs.

A suitable size of clusters for Step 2 was investigated. An intpTAC should be a monotonically increasing function with positive values. The failed curves in Step 5 mean the intpTACs with negative values or the intpTACs that do not monotonically increase. In Step 5, a scale of the intpTAC should be normalized before averaging because it cannot be determined using ISA.

## Materials and methods

### *Simulations*

Simulations were carried out to investigate the behavior of the ISA in the presence of noise to make sure of the necessity of noise reduction in applying ISA. Perfect tTACs were generated using a metabolite-corrected pTAC obtained from a human [$^{11}$C]TMSX study with serial arterial blood sampling. Kinetic parameter values of [$^{11}$C]TMSX in the putamen and the frontal lobe (Naganawa et al., 2007b) were chosen for the generation of noise-free tTACs ($K_1$=0.32 (mL plasma)·min$^{-1}$ (mL tissue)$^{-1}$, $k_2$=0.43 min$^{-1}$, $k_3$=0.44 min$^{-1}$, $k_4$=0.36 min$^{-1}$ and $K_1$=0.29 (mL plasma)·min$^{-1}$ (mL tissue)$^{-1}$, $k_2$=0.39 min$^{-1}$, $k_3$=0.13 min$^{-1}$, $k_4$=0.29 min$^{-1}$, respectively). Noisy data were subsequently obtained by adding Gaussian noise to the noise-free data. Added noise was expressed as $\mathcal{N}\left(0, \beta\frac{c(t)}{\Delta t}\right)$, where $\Delta t$ is the frame width and $\beta$ is a proportional constant that represents the noise level. The simulations were conducted for a protocol of 27 frames over a period of 1 h (10 s × 6, 30 s × 3, 60 s × 5, 150 s × 5, and 5 min × 8). The noise level $\beta$ was set to be 0 and 16. The noise level was scaled so that the value of 16 corresponded to the averaged tTAC over 100 voxels. In the simulation, 20 realizations of noisy tTACs were generated, and 10 pairs of tTACs were randomly selected from the tTACs, and ISA was applied to them because an intpTAC is estimated using two tTACs in EPISA. ISA was also applied to noise-free tTACs. Because it is possible to apply Logan plots to [$^{11}$C]TMSX 10 min after administration (Naganawa et al., 2007b), ISA was performed using the simulated data between 27.5 and 57.5 min after administration. The estimated intpTACs were compared with the true intpTAC.

### *[$^{11}$C]TMSX PET studies*

The presented method (robust EPISA) was applied to eight human [$^{11}$C]TMSX PET data sets in order to investigate the effects of averaging and clustering. The Ethics Committee of Tokyo Metropolitan Institute of Gerontology approved the study protocol. [$^{11}$C]TMSX PET data were acquired from seven healthy volunteers and one patient with Parkinson's disease. Written informed consent was obtained from all subjects before the study. After a transmission scan, 590 ± 103 MBq of [$^{11}$C]TMSX with a specific activity of 40 ± 21 GBq/μmol was administered intravenously, and a 1 h dynamic PET scan was performed in two-dimensional mode using a SET-2400W (Shimadzu Co., Kyoto, Japan). The acquisition consisted of 27 frames of data (10 s × 6, 30 s × 3, 60 s × 5, 150 s × 5, and 5 min × 8). The dynamic PET data were reconstructed using a filtered back-projection algorithm with a second-order low-pass filter with a cutoff frequency of 1.25 cycles/cm. Twenty-five slices were scanned–each slice with 96 × 96 voxels–and the resulting voxel size was 2 × 2 × 6.25 mm. Serial arterial blood sampling and metabolite analysis were performed during the scan. Arterial blood samples were taken from the brachial artery at 10, 20, 30, 40, 50, 60, 70, 80, 90, 100, 110, 120, 135 and 150 s and 3, 5, 7, 10, 15, 20, 30, 40, 50 and 60 min. The radioactivity in the plasma was measured using a well-type gamma counter (BSS-1, Shimadzu Co., Kyoto, Japan) against which the PET camera was cross-calibrated. The unmetabolized fraction was measured by high-performance liquid chromatography (Ishiwata et al., 2003). The unmetabolized fraction in the plasma samples was fitted to the function proposed in Watabe et al. (2000).

Fifteen slices that cover the whole brain were used for estimation by robust EPISA. The regions outside the brain were specified as the voxels below the 70th percentile of the summed PET images and were excluded from the target of the robust EPISA. Approximately 63,000 voxels were used for the estimation. The 5-by-5 average filter was applied to the measured PET images to improve the signal-to-noise ratio by spatial averaging. The number of clusters was set to 50, and approximately 1250 voxels were included in one cluster. Thus, sufficiently noise-reduced tTACs were obtained. PET images taken between 27.5 and 57.5 min after administration were used in the ISA. The estimated intpTAC was divided by its value at the last frame for normalization. Logan plot was applied to obtain the $V_T$ image using the metabolite-corrected intpTAC and the estimated intpTAC. The centrum semiovale was manually defined as a reference region, and the binding potential, $BP_{ND}$, image was given by $\frac{V_T}{V_{ND}} - 1$ where $V_{ND}$ is the averaged $V_T$ over the centrum semiovale.

### *[$^{11}$C]PIB PET studies*

The peripheral metabolism of [$^{11}$C]TMSX is slow; more than 95% of administered [$^{11}$C]TMSX remains as the intact form at 60 min post injection (Naganawa et al., 2007b). Therefore, the measured pTACs with and without metabolite correction have similar shape in [$^{11}$C]TMSX data. In order to investigate the influence of metabolites included in plasma and the number of clusters, the robust EPISA was also applied to four human [$^{11}$C] PIB PET data sets with faster metabolism. Parent fraction of [$^{11}$C] PIB was 48 ± 13% at 20 min and 30 ± 8% at 60 min post injection. The Ethics Committee of Tokyo Metropolitan Institute of Gerontology approved the study protocol. [$^{11}$C]PIB PET data were acquired from two healthy volunteers and two patients with Alzheimer disease who met the criteria of probable AD by NINDS-ADRDA and Dementia of Alzheimer's Type with DSM-IV. Written informed consent was obtained from all subjects before the study. After a transmission scan, 455 ± 55 MBq of [$^{11}$C]PIB with a specific activity of 88 ± 32 GBq/μmol was administered intravenously, and a 1 h dynamic PET scan was performed in three-dimensional mode using the same scanner as [$^{11}$C]TMSX scan. The acquisition consisted of 23 frames of data (10 s × 6, 20 s × 3, 60 s × 2, 2 min × 1, 4 min × 1, and 5 min × 10). Image reconstruction, serial arterial blood sampling and metabolite analysis were conducted in the same way as [$^{11}$C]TMSX scan, and 50 slices were scanned.

Slices that cover the whole brain were used for estimation by robust EPISA. The regions outside the brain were specified as the voxels below the 80th percentile of the summed PET images and were excluded from the target of the robust EPISA. Approximately 126,000 voxels were used for the estimation. The 9-by-9 average filter was applied to the measured PET images. The number of clusters was set to 10 (12,600 voxels/cluster), 20 (6300 voxels/cluster), 40 (3150 voxels/cluster) and 80 (1575 voxels/cluster). ISA was applied to PET images taken between 37.5 and 57.5 min after administration (Price et al., 2005; Lopresti et al., 2005). The estimated intpTAC was divided by its value at the last frame for normalization. Logan plot was applied to obtain the $V_T$ image using the metabolite-corrected intpTAC and the estimated intpTAC. The cerebellum was manually defined as a reference region (Price et al., 2005), and the distribution volume ratio (DVR) image was calculated.

## Results

### *Simulation*

The noise sensitivity of the ISA was confirmed using the simulated [$^{11}$C]TMSX data. The noise-free tTACs and examples of noise-added tTACs used for the simulation are presented in Fig. 2. Fig. 3 shows the estimated intpTACs and the true intpTAC. The scale was adjusted so that the value at the last frame corresponds to that of the true intpTAC. There was no difference between the ISA-estimated intpTAC and the true intpTAC with noise-free data. However, the estimated intpTACs were apparently deviated from the true intpTAC with a noise level of 16.

### *[$^{11}$C]TMSX PET studies*

Clustering results are shown in Figs. 4 and 5. In Fig. 5, the voxels that have larger clustering criterion $R$ are represented in a brighter color. While the neighboring voxels tend to belong to the same cluster and brain structure can be observed in Fig. 5, some remote voxels were also categorized into the same cluster. The intpTAC was estimated from the clustered and averaged tTACs as shown in Fig. 4. The noise level in the cluster-averaged tTACs was well suppressed. The estimated intpTACs using the proposed robust EPISA is demonstrated with standard deviation in Fig. 6(A). Note that standard deviation was not calculated from all estimated intpTACs but the candidate intpTACs as described in Step 5 in the Robust EPISA section. The estimated intpTACs were similar to the measured intpTACs with metabolite correction. The scale of the robust EPISA estimated intpTAC cannot be determined. In order to compare the estimated intpTACs with the measured intpTACs, the estimated intpTACs were scaled using the value at the last frame. The measured intpTACs without metabolite correction were also scaled using the value at the last frame. It took 5 to 7 s to estimate the intpTAC from one subject's data. The Logan plot was applied to the measured PET data to generate the $V_T$ parametric images, and Fig. 7 shows $BP_{ND}$ images calculated using the estimated $V_T$

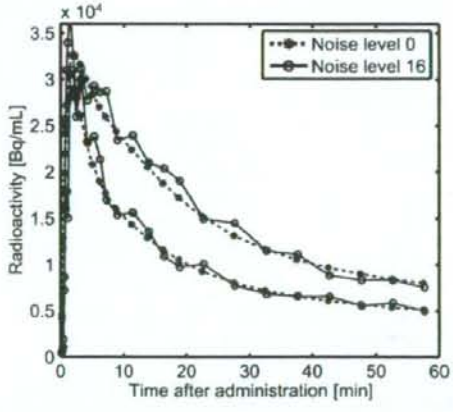


Fig. 2. Example of noise-free tTACs (dashed lines) and noisy tTACs (solid lines) for the simulation investigating the influence of noise in tTACs. The noise level of the noisy tTACs was set to 16. Two kinds of tTACs were used for estimation using ISA.

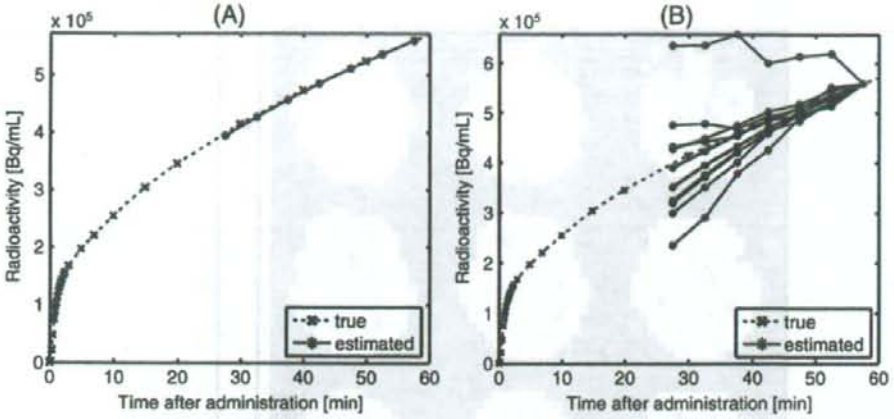


Fig. 3. Estimated intpTACs from the noise-free data (A) and the noisy data (B). The period used for the ISA was 27.5 min to 57.5 min after administration. The true intpTAC was obtained by cumulatively integrating the true pTAC. The estimated intpTACs are shown as solid lines, and the true intpTACs are shown as dashed lines. The scale of the estimated intpTAC was adjusted using the value at the last frame.

parametric images and the specified reference region. The $BP_{ND}$ images with the estimated and measured intpTACs matched well in all eight subjects. In the linear regression between the measured and estimated $BP_{ND}$ images, the slopes and $y$-intercepts were $1.00\pm0.011$ and $0.035\pm0.016$, respectively. The coefficient of determination ($r^2$) was $1.00\pm0.0016$.

### *[$^{11}$C]PIB PET studies*

Fig. 6(B) shows the estimated intpTAC and the standard deviation calculated from candidate intpTACs. The estimated intpTACs were similar to the measured intpTACs with metabolite correction. For comparison, the scale of the estimated intpTACs and the measured intpTACs without metabolite correction was adjusted using the value at the last frame of the measured intpTACs

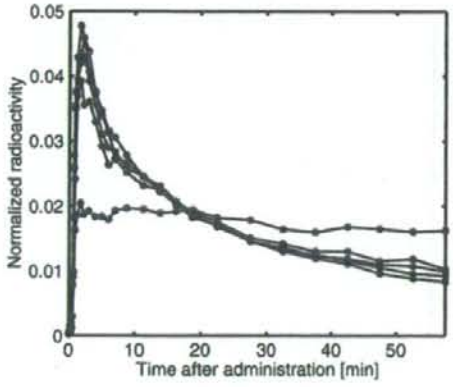


Fig. 4. Representative tTACs after clustering in [$^{11}$C]TMSX data. The tTACs of the measured PET data were categorized into 50 clusters and subsequently averaged in each cluster. Each tTAC was normalized by dividing by its integral.

with metabolite correction. The calculation time was comparable to [$^{11}$C]TMSX study. The relationship between the number of clusters and estimation results were demonstrated in Fig. 8. Standard deviation increased as the size of the clusters became smaller. However, the final estimated intpTAC was little influenced by the choice of the number of clusters. In each case with different number of clusters, the candidate intpTACs from which the final result was obtained were approximately 22% curves out of all estimated intpTACs. When the number of the clusters set to be less than 5, the proposed method did not work. The Logan plot was applied to the measured PET data to generate the $V_T$ parametric images, and Fig. 9 shows the DVR images of Alzheimer disease patient that were calculated using the estimated $V_T$ parametric images in case of 20 clusters. The DVR images with the estimated and measured intpTACs matched well in all four subjects. In the linear regression between the measured and estimated DVR images, the slopes and $y$-intercepts were $0.97\pm0.038$ and $0.060\pm0.057$, respectively. The coefficient of determination ($r^2$) was $0.97\pm0.026$.

## Discussion

The proposed method, robust EPISA, settles the mathematical drawback in ISA, in that performance is influenced by the noise in the measured tTACs. The measurement noise included in PET data was reduced by clustering based on tTAC's kinetics, and an input function for Logan plots was estimated robustly based on ISA (Wang et al., 2005). Robust EPISA estimates a shape of a cumulative integral curve of pTAC appearing in the operational equation of the Logan plot, and enables binding-potential imaging to be generated with no arterial blood sampling or metabolite correction. Omission of arterial blood sampling reduces the invasiveness of PET measurement and contributes to the shortened total time needed for preparation of serial arterial blood sampling. Before discussing the robustness of the proposed method, we should consider the advantages and disadvantages of ISA.

ISA has two advantages: no requirement for metabolite correction of pTAC and wide applicability to PET data with various radioligands, because of the broad application of the Logan

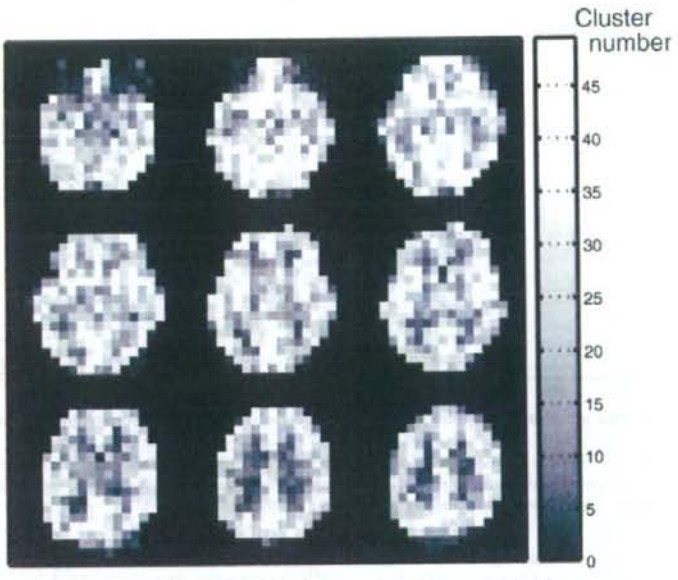


Fig. 5. Example of a clustered image in [$^{11}$C]TMSX data. The voxel value corresponds to the cluster number. As the cluster number becomes larger, the corresponding criterion $R$ also becomes larger.

plot. Many methods have been proposed to preclude arterial blood sampling. One of these methods is based on a factor model to estimate the shape of a whole blood curve (Barber, 1980; Paola et al., 1982; Wu et al., 1995; Lee et al., 2001; Naganawa et al., 2005a,b), where the radioactivity in the measured PET data is assumed to be the sum of the radioactivities in the blood and tissue. In this method, metabolite correction is unattainable. On the other hand, ISA can theoretically give a metabolite-corrected pTAC. ISA is derived from the operational equation for the Logan plot, and the equations of the Logan plot are based on a compartment model. Thus, the estimated intpTAC does not include the radioactivity in metabolites. There is a great difference between the measured intpTAC with and without metabolite correction in [$^{11}$C]PIB data. The estimated intpTAC matched well with the measured intpTAC with metabolite correction as shown in Fig. 6. From our results, the estimated $BP_{ND}$ of [$^{11}$C]TMSX (Fig. 7) or DVR of [$^{11}$C]PIB (Fig. 9) using the proposed method coincide well with those using a measured pTAC with metabolite correction. It is expected that ISA

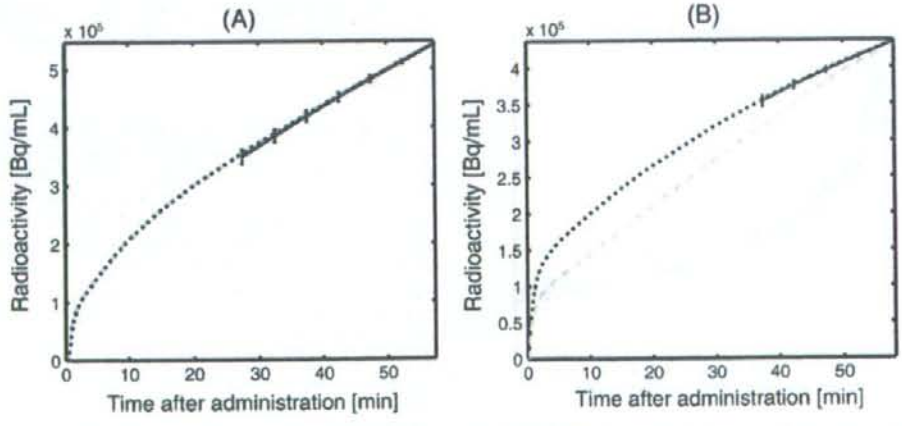


Fig. 6. Example of a robust EPISA-estimated intpTAC (black solid line) in (A) [$^{11}$C]TMSX and (B) [$^{11}$C]PIB. In [$^{11}$C] PIB, 40 clusters were used for clustering. Measured intpTACs with and without metabolite correction were plotted in black dotted line and gray break line, respectively. Standard deviation was calculated from the candidate intpTACs.

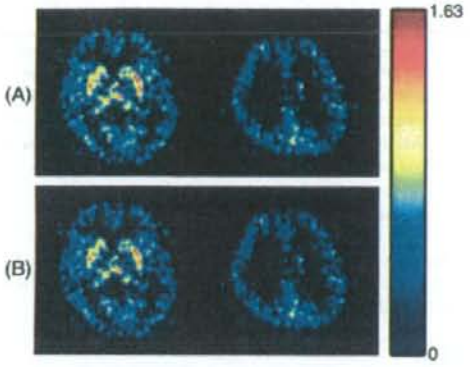


Fig. 7. Example of the parametric images of the $BP_{ND}$ in [$^{11}$C]TMSX PET data using the robust EPISA-estimated intpTAC (A) and the measured intpTAC with metabolite correction (B). These images were calculated from the $V_t$ images and a reference region.

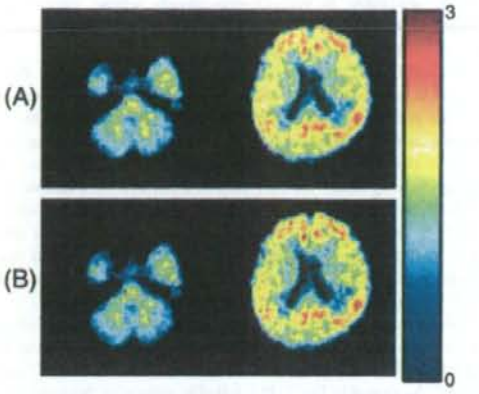


Fig. 9. Example of the parametric images of [$^{11}$C]PIB DVR in brain with Alzheimer disease. These images were calculated from the $V_t$ images and a reference region using the robust EPISA-estimated intpTAC (A) and the measured intpTAC with metabolite correction (B).

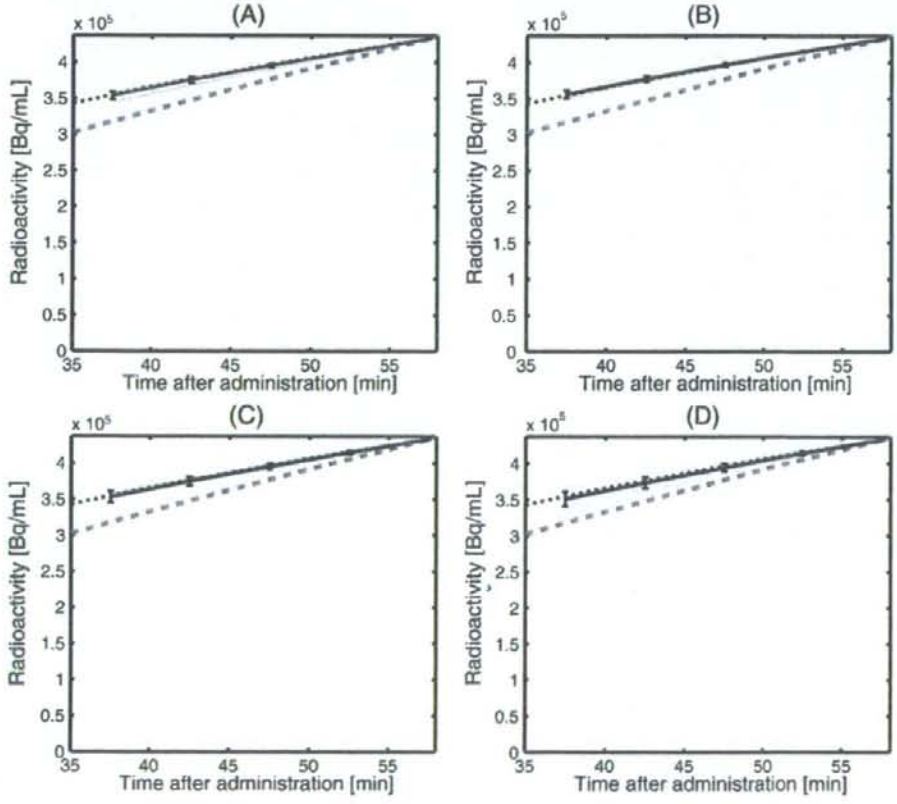


Fig. 8. Typical example of robust EPISA-estimated intpTACs (black solid line) in [$^{11}$C]PIB. The number of clusters was set to (A) 10, (B) 20, (C) 40, and (D) 80. Measured intpTACs with and without metabolite correction were plotted in black dotted line and gray break line. Standard deviation was calculated from the candidate intpTACs that were shown in gray solid lines.

will be applicable to radiopharmaceuticals whose metabolites cannot be ignored, or PET data with metabolism varied because of disease, dose, or other pathophysiological situations.

The next issue is the wide applicability of ISA. Using ISA, parametric images of $BP_{ND}$ can be calculated using the estimated intpTAC and the specified reference region. When arterial blood sampling is not available, the basis function method (Gunn et al., 1997) is commonly used. While the basis function method is appropriate only when the PET data is described by a simplified reference tissue model (Lammertsma and Hume, 1996), ISA can be applied to any PET data with reversibly binding tracers. In this paper, to assure the wide applicability, EPISA was applied to two radioligands: [$^{11}$C]TMSX with slow peripheral metabolism and [$^{11}$C]PIB with fast one.

ISA has a disadvantage in practical application because of its high sensitivity to measurement noise. ISA is an algorithm to estimate the intersection between the planes spanned by tTAC and inttTAC. As shown in Fig. 3, ISA failed in estimating the intpTAC, even with low-noise. The reason for this is considered here. The ISA algorithm leads to the singular value decomposition problem. Generally, the singular vector with the smallest singular value is inaccurately estimated in the presence of noise. Therefore, it is important to reduce noise from the measured PET data before applying ISA.

In addition, the absolute value of the intpTAC cannot be estimated using ISA, as with other mathematical algorithms for the pTAC estimation (Barber, 1980; Paola et al., 1982; Wu et al., 1995; Lee et al., 2001; Naganawa et al., 2005a,b), because only the direction of a singular vector is presumable. Therefore, the relative $V_T$ is obtained using Logan plot with the estimated pTAC or intpTAC. At least one-point arterial blood sampling is required to scale the estimated pTAC or intpTAC and calculate the absolute $V_T$. However, $BP_{ND}$ can be calculated from the ratio of $V_T$ values between target voxels and the reference region, and this calculation does not require the absolute value of the intpTAC. ISA can form the parametric image of $BP_{ND}$ by specifying reference region.

In this study, a kinetic model-based clustering scheme was applied for noise reduction. It has been successfully applied in the rapid and robust parametric imaging of regional cerebral blood flow (Kimura et al., 1999) and [$^{18}$F]FDG studies (Kimura et al., 2002). In this paper, we proposed averaging and clustering as a way to successful ISA. The measured tTACs were clustered based on their kinetic shape. In the [$^{11}$C]TMSX studies, approximately 1250 voxels were assigned to a single cluster. Although the size of the cluster is too large as an anatomical ROI, such a large ROI is appropriate for EPISA because reducing noise is more important than increasing heterogeneity in the clusters. The estimated result was not influenced too much by the choice of the number of the clusters as shown in Fig. 8. IntpTACs were estimated from all possible pairs of the noise-reduced tTACs. In some pairs, estimated intpTAC's were not monotonically increasing. The derivative of the intpTAC equals the pTAC. Therefore, the pTAC includes negative values when the intpTAC was not monotonically increasing.

The reference-region-based Logan plot also successfully estimates DVR or $BP_{ND}$ without arterial blood sampling. Comparing EPISA with the reference-region-based Logan plot, robust EPISA does not need any kinetic parameters, while the reference-region-based Logan plot requires the population value of $k_2$ in the reference region in advance. We think that it is an advantage over the noninvasive Logan analysis. Note that noninvasive Logan analysis and our method will provide comparable results when the values of $k_2$ in a reference region are sufficiently similar in all subjects.

Exact values should be specified for the set of parameters used in the robust EPISA: the size of the averaging filter and the number of clusters. When the PET data have a low signal-to-noise ratio, a larger averaging filter and fewer clusters are preferable. We conclude that the ISA is a practical algorithm for the obviation of arterial blood sampling using noise reduction with clustering.

## Acknowledgments

This work was supported in part by Grants-in-Aid for Scientific Research of the Japan Society for the Promotion of Science, No. 18591373 in 2006–2007, and No. 18-6916 in 2006–2008.

## References

Barber, D.C., 1980. The use of principal components in the quantitative analysis of gamma camera dynamic studies. Phys. Med. Biol. 25 (2), 283–292.

Carson, R.E., 2002. Positron Emission Tomography Basic Science and Clinical Practice. Springer, Ch. 6, pp. 147–179.

Gunn, R.N., Lammertsma, A.A., Hume, S.P., Cunningham, V.J., 1997. Parametric imaging of ligand–receptor in PET using a simplified reference region model. NeuroImage 6 (4), 279–287.

Innis, R.B., Cunningham, V.J., Delforge, J., Fujita, M., Gjedde, A., Gunn, R.N., Holden, J., Houle, S., Huang, S.-C., Ichise, M., Iida, H., Ito, H., Kimura, Y., Koeppe, R.A., Knudsen, G.M., Knuuti, J., Lammertsma, A.A., Laruelle, M., Logan, J., Maguire, R.P., Mintun, M.A., Morris, E.D., Parsey, R., Price, J.C., Slifstein, M., Sossi, V., Suhara, T., Votaw, J.R., Wong, D.F., Carson, R.E., 2007. Consensus nomenclature for *in vivo* imaging of reversibly binding radioligands. J. Cereb. Blood Flow Metab. 27 (9), 1533–1539.

Ishiwata, K., Ogi, N., Shimada, J., Nonaka, H., Tanaka, A., Suzuki, F., Senda, M., 2000. Further characterization of a CNS adenosine $A_{2a}$ receptor ligand [$^{11}$C]KF18446 with *in vitro* autoradiography and *in vivo* tissue uptake. Ann. Nucl. Med. 14 (2), 81–89.

Ishiwata, K., Wang, W.-F., Kimura, Y., Kawamura, K., Ishii, K., 2003. Preclinical studies on [$^{11}$C]TMSX for mapping adenosine $A_{2A}$ receptors by positron emission tomography. Ann. Nucl. Med. 17 (3), 205–211.

Ishiwata, K., Mishina, M., Kimura, Y., Oda, K., Sasaki, T., Ishii, K., 2005. First visualization of adenosine $A_{2A}$ receptors in the human brain by positron emission tomography with [$^{11}$C]TMSX. Synapse 55 (2), 133–136.

Kimura, Y., Hsu, H., Toyama, H., Senda, M., Alpert, N.M., 1999. Improved signal-to-noise ratio in parametric images by cluster analysis. NeuroImage 9 (5), 554–561.

Kimura, Y., Senda, M., Alpert, N.M., 2002. Fast formation of statistically reliable FDG parametric images based on clustering and principal components. Phys. Med. Biol. 47 (3), 455–468.

Kimura, Y., Naganawa, M., Yano, J., 2005a. Multidimensional clustering for molecular imaging using positron emission tomography and Logan plot to improve noise reduction capability. Proceedings of the International Federation for Medical and Biological Engineering, vol. 12, p. 2A2-01. Singapore.

Kimura, Y., Yano, J., Tsukahara, M., Naganawa, M., Ishii, K., Ishiwata, K., 2005b. Clustering approach for voxel-based Logan plot to improve noise reduction capability. VIIth International Conference on Quantification of Brain Function with PET. Amsterdam, Netherlands. p. S632.

Klunk, W.E., Engler, H., Nordberg, A., Wang, Y., Blomqvist, G., Holt, D.P., Bergström, M., Savitcheva, I., Huang, G.-F., Estrada, S., Ausén, B., Debnath, M.L., Barletta, J., Price, J.C., Sandell, J., Lopresti, B.J., Wall, A., Koivisto, P., Antoni, G., Mathis, C.A., Långström, B., 2004. Imaging brain amyloid in Alzheimer's disease with Pittsburgh Compound-B. Ann. Neurol. 55 (3), 306–319.

Koeppe, R.A., Holthoff, V.A., Frey, K.A., Kilbourn, M.R., Kuhl, D.E., 1991.

Compartmental analysis of [$^{11}$C]flumazenil kinetics for the estimation of ligand transport rate and receptor distribution using positron emission tomography. J. Cereb. Blood Flow Metab. 11 (5), 735–744.

Lammertsma, A.A., Hume, S.P., 1996. Simplified reference tissue model for PET receptor studies. NeuroImage 4, 153–158.

Lee, J.S., Lee, D.S., Ahn, J.Y., Cheon, G.J., Kim, S.K., Yeo, J.S., Seo, K., Park, K.S., Chung, J.K., Lee, M.C., 2001. Blind separation of cardiac components and extraction of input function from $H_2{}^{15}O$ dynamic myocardial PET using independent component analysis. J. Nucl. Med. 42 (6), 938–943.

Logan, J., Fowler, J.S., Volkow, N.D., Wolf, A.P., Dewey, A.L., Schlyer, D.J., MacGregor, R.R., Hitzeman, R., Bendriem, B., Gatley, S.J., Christman, D.R., 1990. Graphical analysis of reversible radioligand binding from time–activity measurements applied to [*n*-$^{11}$C-methyl]-(−)-cocaine PET studies in human subjects. J. Cereb. Blood Flow Metab. 10 (5), 740–747.

Logan, J., Fowler, J.S., Volkow, N.D., Wang, G.-J., Ding, Y.-S., Alexoff, D.L., 1996. Distribution volume ratios without blood sampling from graphical analysis of PET data. J. Cereb. Blood Flow Metab. 16 (5), 834–840.

Lopresti, B.J., Klunk, W.E., Mathis, C.A., Hoge, J.A., Ziolko, S.K., Lu, X., Meltzer, C.C., Schimmerl, K., Tsopelas, N.D., DeKosky, S.T., Price, J.C., 2005. Simplified quantification of Pittsburgh Compound B amyloid imaging PET studies: a comparative analysis. J. Nucl. Med. 46 (12), 1959–1972.

Mathis, C.A., Wang, Y., Holt, D.P., Huang, G.-F., Debnath, M.L., Klunk, W.E., 2003. Synthesis and evaluation of $^{11}$C-labeled 6-substituted 2-arylbenzothiazoles as amyloid imaging agents. J. Med. Chem. 46 (13), 2740–2754.

Mishina, M., Ishiwata, K., Kimura, Y., Naganawa, M., Oda, K., Kobayashi, S., Katayama, Y., Ishii, K., 2007. Evaluation of distribution of adenosine $A_{2A}$ receptors in normal human brain measured with [$^{11}$C]TMSX PET. Synapse 61 (9), 778–784.

Naganawa, M., Kimura, Y., Ishii, K., Oda, K., Ishiwata, K., Matani, A., 2005a. Extraction of a plasma time–activity curve from dynamic brain PET images based on independent component analysis. IEEE Trans. Biomed. Eng. 52 (2), 201–210.

Naganawa, M., Kimura, Y., Nariai, T., Ishii, K., Oda, K., Manabe, Y., Chihara, K., Ishiwata, K., 2005b. Omission of serial arterial blood sampling in neuroreceptor imaging with independent component analysis. NeuroImage 26 (3), 885–890.

Naganawa, M., Kimura, Y., Ishii, K., Oda, K., Ishiwata, K., 2007a. Temporal and spatial blood information estimation using Bayesian ICA in dynamic cerebral positron emission tomography. Digit. Signal Process. 17 (5), 979–993.

Naganawa, M., Kimura, Y., Mishina, M., Manabe, Y., Chihara, K., Oda, K., Ishii, K., Ishiwata, K., 2007b. Quantification of adenosine $A_{2A}$ receptors in the human brain using [$^{11}$C]TMSX and positron emission tomography. Eur. J. Nucl. Med. Mol. Imaging 34 (5), 679–687.

Di Paola, R., Bazin, J.P., Aubry, F., Aurengo, A., Cavailloles, F., Herry, J.Y., Kahn, E., 1982. Handling of dynamic sequences in nuclear medicine. IEEE Trans. Nucl. Sci. NS-29 (4), 1310–1321.

Price, J.C., Klunk, W.E., Lopresti, B.J., Lu, X., Hoge, J.A., Ziolko, S.K., Holt, D.P., Meltzer, C.C., DeKosky, S.T., Mathis, C.A., 2005. Kinetic modeling of amyloid binding in humans using PET imaging and Pittsburgh Compound-B. J. Cereb. Blood Flow Metab. 25 (11), 1528–1547.

Wang, Z.J., Peng, Q., Liu, K.J.R., Szabo, Z., 2005. Model-based receptor quantization analysis for PET parametric imaging. 27th Annual International Conference of the IEEE Engineering in Medicine and Biology Society, pp. 5908–5911.

Watabe, H., Channing, M.A., Der, M.G., Adams, H.R., Jagoda, E., Herscovitch, P., Eckelman, W.C., Carson, R.E., 2000. Kinetic analysis of the 5-$HT_{2A}$ ligand [$^{11}$C]MDL 100,907. J. Cereb. Blood Flow Metab. 20, 899–909.

Wu, H.M., Hoh, C.K., Choi, Y., Schelbert, H.R., Hawkins, R.A., Phelps, M.E., Huang, S.C., 1995. Factor analysis for extraction of blood time–activity curves in dynamic FDG-PET studies. J. Nucl. Med. 36 (9), 1714–1722.

ELSEVIER

Journal of the Neurological Sciences 268 (2008) 102–107

Journal of the Neurological Sciences

www.elsevier.com/locate/jns

# Measurement of the $^{11}$C-flumazenil binding in the visual cortex predicts the prognosis of hemianopia

Yukihisa Suzuki [a,b], Chiharu Horie [a,b], Motohiro Kiyosawa [a,b], Tadashi Nariai [b,c], Manabu Mochizuki [a], Keiichi Oda [b], Yuichi Kimura [b], Kiich Ishiwata [b], Kenji Ishii [b,*]

[a] *Department of Ophthalmology and Visual Science, Tokyo Medical and Dental University, Graduate School, Tokyo, Japan*
[b] *Positron Medical Center, Tokyo Metropolitan Institute of Gerontology, Tokyo, Japan*
[c] *Department of Neurosurgery, Tokyo Medical and Dental University, Graduate School, Tokyo, Japan*

Received 10 September 2007; received in revised form 17 November 2007; accepted 21 November 2007
Available online 9 January 2008

**Abstract**

In order to determine whether functional neuroimaging studies can predict the prognosis of hemianopia due to organic cerebral disorders, we studied 8 patients (6 men and 2 women; age, 56.0±8.6 years) with homonymous hemianopia and compared them with 15 normal subjects (6 men and 9 women; age, 54.3±4.4 years). The cerebral glucose metabolism and $^{11}$C-flumazenil (FMZ) binding were measured by positron emission tomography, more than 1 month after the onset of the condition. Bilateral regions of interest (ROIs) were selected in the striate cortex, extrastriate cortex, cuneus and thalamus. Further, semi-quantitative data on the cerebral glucose metabolism and FMZ binding were obtained for the ROIs and compared with the data obtained for homologous regions in the contralateral hemisphere by calculating the ipsilateral/contralateral (*I/C*) ratio. The *I/C* ratios for the cerebral glucose metabolism and FMZ binding in the striate cortex were significantly low in the patients (glucose metabolism, $P<0.0005$; FMZ binding, $P<0.005$), while the ratio for the FMZ binding in the cuneus increased ($P<0.0005$). We observed that 5 patients, whose *I/C* ratio for the FMZ binding in the striate cortex was >0.850, experienced an improvement in their visual field, while that 3 patients with lower *I/C* ratios did not. The FMZ-PET may be useful to predict the prognosis of hemianopia in the chronic phase.


*Keywords:* Central benzodiazepine receptor; Cerebral glucose metabolism; Hemianopia; Prognosis; Positron emission tomography; Visual field

## 1. Introduction

Damage to the visual cortex or the geniculostriate pathways produces homonymous visual field defects contralateral to the side of the lesion. In clinical practice, it is known that the visual field defects improve gradually over some months in most cases. Recently, diffusion-weighted magnetic resonance imaging (MRI) has been used for the evaluation of acute ischemic cerebral lesions [1]. Positron emission tomography (PET) with $^{18}$F-fluorodeoxyglucose (FDG) has been used to study clinical–metabolic correlations in patients with ischemic lesions of the visual cortex or optic radiations [2]. However, it is difficult to estimate the prognosis of the visual field solely by early FDG-PET findings, due to the occurrence of diaschisis. Previous studies have shown that regions with metabolic abnormalities in the occipital cortex are generally larger than the corresponding anatomic defect appearing on computed tomography (CT) or MR images. Several hypotheses have been proposed to explain the recovery of lost function. However, the neurorepair mechanisms associated with such visual reorganization remain unknown.

The γ-aminobutyric acid (GABA), receptors are abundant in the cerebral cortex and are sensitive to ischemic damage; therefore, the central benzodiazepine receptor (cBZR) density can be used as a marker of preserved morphological integrity. An animal study provided evidence that alterations occur in

* Corresponding author. Positron Medical Center, Tokyo Metropolitan Institute of Gerontology, 35-2 Sakae-cho, Itabashi, Tokyo, 173-0022, Japan. Tel.: +81 3 3964 3241x3503; fax: +81 3 3964 2188.
*E-mail address:* ishii@pet.tmig.or.jp (K. Ishii).

0022-510X/$ - see front matter © 2007 Elsevier B.V. All rights reserved.
doi:10.1016/j.jns.2007.11.017

the GABAergic system following ischemic lesion protocol [3,4]. In our previous study, by performing $^{11}$C-flumazenil (FMZ)-PET, we measured the density of the central benzodiazepine–$GABA_A$ receptor complex in a patient with hemianopia caused by multiple sclerosis [5]. Further, Heiss et al. reported that the reversibility of ischemic cortical damage in acute stroke patients can be predicted by performing FMZ-PET [6]. However, there has been no report regarding the relationship between the visual field and the cBZR density of the visual cortex in humans. We examined whether measurement of the cerebral glucose metabolism and cBZR density of hemianopia patients by performing FDG-PET and FMZ-PET, respectively, can be used to estimate the prognosis of the visual field. The PET examinations were performed more than 1 month after the onset of the condition in order to exclude any influence of diaschisis; further Goldmann kinetic perimetry was performed 2 years after the onset and prior to the PET diagnosis.

## 2. Materials and methods

We studied 8 patients (6 men and 2 women; age, 56.0± 8.6 years) with homonymous visual field defects caused by cerebral lesions of the posterior afferent visual system (Table 1). The patients visited the Ophthalmology Outpatient Clinic of Tokyo Medical and Dental University Hospital. All patients had a corrected visual acuity of 20/30 or better in both eyes. Goldmann kinetic perimetry was performed prior to PET scanning. Patients 1, 2, 4, 5, and 8 had right homonymous hemianopia, while patients 3, 6, and 7 had left homonymous hemianopia (Table 1). The only clinical symptom in patients 1, 2, 3, 4, and 5 was homonymous hemianopia. However, in additional to hemianopia, patient 6 had numbness in the right side of the body; patient 7, aphasia and hemiparesis; and patient 8, hemispatial neglect.

Informed consent was obtained from all the subjects prior to their participation in the PET study. The study protocol was approved by the Institutional Ethics Committee. All the procedures conformed to the tenets of the Declaration of Helsinki.

To study the cerebral lesions, MRI scans were obtained from all of the patients by using a 1.5-Tesla Signa Horizon scanner (General Electric, Milwaukee, WI). Transaxial images with T1-weighted contrast (3DSPGR, TR=9.2 ms, TE=2.0 ms, matrix size=256×256×124, voxel size=0.94×0.94×1.3 mm) and T2-weighted contrast (First Spin Echo, TR=3000 ms, TE=100 ms, matrix size=256×256×20, voxel size=0.7×0.7×6.5 mm) were obtained.

For all the patients, FDG- and FMZ-PET scans were performed on a single day. To exclude any influence of diaschisis, we performed these PET scans at least 1 month after the organic event. After 2 years from the onset of hemianopia symptoms, Goldmann kinetic perimetry was performed once again for all the patients.

### 2.1. PET data acquisition

PET scans were obtained using the SET 2400 W whole-body scanner (Shimadzu, Kyoto, Japan) at the Positron Medical Center, Tokyo Metropolitan Institute of Gerontology.

For the FDG-PET scan, a bolus of 2.5 MBq/kg (body weight) [$^{18}$F] FDG was injected intravenously. Each patient was then requested to lie down comfortably with eyes closed. A 6-minute emission scan in the 3D acquisition mode was initiated 45 min after the injection, and 50 transaxial images with an interslice interval of 3.125 mm were obtained. The tomographic images were reconstructed by the filtered backprojection method using a Butterworth filter (cut-off frequency, 1.25 cycle/cm; order, 2).

The FMZ binding data were acquired in the 3D acquisition mode by performing a static scan from 20 to 40 min after the intravenous injection of 6.0 MBq/kg (body weight) FMZ [7]. The specific activity and amount of the injected cold material were 54.0±59.1 MBq/nmol and 14±11 nmol, respectively.

In each PET scan, attenuation was corrected by performing a transmission scan using a $^{68}$Ga/$^{68}$Ge rotating source.

### 2.2. Data processing

PET images were registered three-dimensionally to the individual 3DSPGR MRIs with the Automated Medical Images Registration (AMIR) program [8]. Further data analysis was performed on LIUX workstations by using the Dr. View program (AJS, Tokyo, Japan). Regions of interest (ROIs), i.e., circles of 1-cm-diameter, were interactively defined on the resliced PET images by visual observation with reference to the corresponding MR image.

Table 1
Injured area of hemianopia patients

| Patient | Age/sex | Description of injury | Cause |
|---|---|---|---|
| 1 | 73/M | A mass lesion in the right lingual gyrus, slight atrophy in the right striate and extrastriate cortex | Brain tumor |
| 2 | 57/F | T1 low/T2 high lesion in the right optic radiation extending to the tapetum | Infarction |
| 3 | 64/F | T1 low/T2 high lesion in the left striate and extrastriate cortex | Infarction |
| 4 | 58/M | T1 low/T2 high lesion in the right cuneus, slight atrophy in the right striate cortex | Infarction |
| 5 | 20/M | T1 low/T2 high lesion in the right optic radiation | Multiple sclerosis |
| 6 | 71/M | T1 low/T2 high lesion in the left striate cortex and lingual gyrus | Infarction |
| 7 | 56/M | T1 low/T2 high lesion in the left striate cortex and left temporal lobe | Infarction |
| 8 | 49/M | T1 low/T2 high lesion in the right striate cortex and bilateral extrastriate cortex | Infarction |

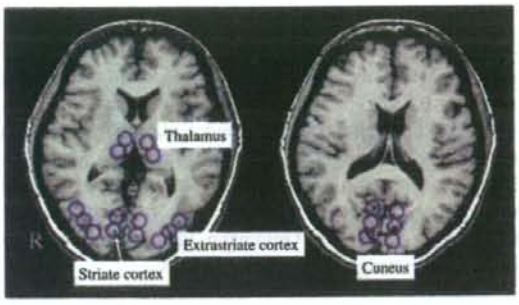


Fig. 1. Bilateral images on which the regions of interest (ROIs) were placed selected namely the striate cortex, extrastriate cortex, cuneus, and thalamus, bilaterally.

Bilateral ROIs were selected in the striate cortex, extrastriate cortex, cuneus, and thalamus, and the cerebral glucose metabolism and FMZ binding in these regions were measured (Fig. 1). The cerebral glucose metabolism and FMZ binding recorded for the ROIs were compared with those recorded for homologous regions in the contralateral hemisphere by calculating the ipsilateral/contralateral (*I/C*) ratio. By taking the ratio in the same brain image, the value is same as the one which measured the value of the quantitative image.

The normal control group comprised 15 healthy volunteers (6 men and 9 women) aged between 48 and 62 years (54.3±4.4 years). MRI and PET scans were obtained for these subjects as in the case of the hemianopia patients. We selected bilateral ROIs on the striate cortex, extrastriate cortex, cuneus, and thalamus, and calculated the *I/C* ratios. The difference in the *I/C* ratios between the patient group and the normal group was tested by performing the Mann–Whitney *U* test with Bonferroni's correction for multiple comparison ($P<0.0125=0.05/4$).

Patients 1 to 7 only exhibited unilateral injuries in the brain. However, patient 8 exhibited unilateral injury in the

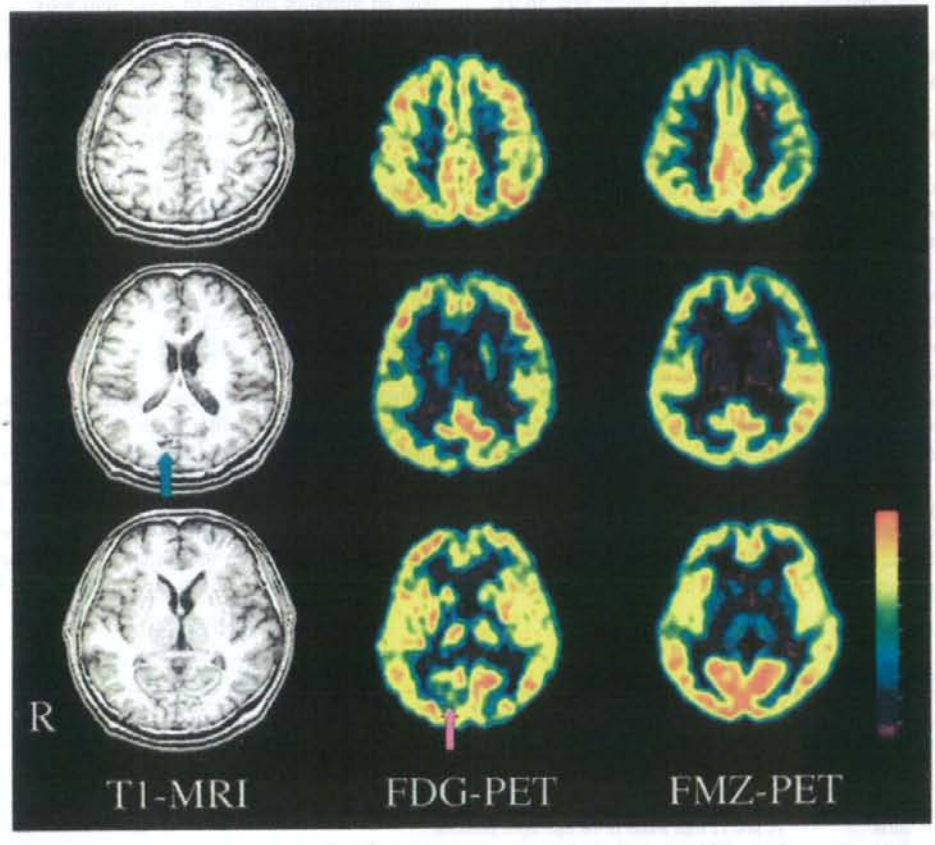


Fig. 2. T1-weighted magnetic resonance (MR) images (left), $^{18}$F-fluorodeoxyglucose (FDG)-positron emission tomography (PET) images (middle), and $^{11}$C-flumazenil (FMZ)-PET images (right) of patient 4. MRI revealed neuronal loss of the right cuneus (green arrow), with decreased FDG and FMZ uptake. The cerebral glucose metabolism decreased in the right striate cortex (pink arrow), while no decrease was observed in the FMZ binding in the striate cortex.

Table 2-A
Ipsilateral/contralateral (*I/C*) ratio for glucose metabolism in each brain region in hemianopia patients

| Patient | Term (month) | Area | | | | VF |
|---|---|---|---|---|---|---|
| | | Striate cortex | Extrastriate cortex | Cuneus | Thalamus | |
| 1 | 1 | 0.809 | 0.632 | 0.965 | 0.987 | Recovered |
| 2 | 1 | 0.765 | 1.020 | 0.649 | 1.007 | Recovered |
| 3 | 2 | 0.852 | 0.453 | 0.939 | 0.933 | Recovered |
| 4 | 3 | 0.769 | 1.045 | 0.998 | 1.030 | Recovered |
| 5 | 1 | 0.862 | 0.894 | 0.849 | 0.892 | Recovered |
| 6 | 3 | 0.568 | 0.706 | 0.862 | 0.863 | Unchanged |
| 7 | 7 | 0.642 | 0.846 | 0.975 | 1.040 | Unchanged |
| 8 | 12 | 0.371 | 0.943[a] | 1.008 | 1.026 | Unchanged |
| Average for patients | | | | | | |
| | | 0.706[b] | 0.817 | 0.907 | 0.972 | |
| | | ±0.168 | ±0.205 | ±0.119 | ±0.068 | |
| Average for normal subjects | | | | | | |
| | | 0.996 | 1.008 | 0.996 | 1.004 | |
| | | ±0.025 | ±0.027 | ±0.036 | ±0.020 | |

VF: visual field.
[a] The extrastriate cortex of patient 8 was damaged bilaterally.
[b] Significantly lower than the value obtained for normal subjects in multiple comparison by the Mann–Whitney *U* test ($P<0.0005$).

striate cortex and bilateral injury in the extrastriate cortex; therefore, *I/C* ratio of the extrastriate cortex may not reflect the visual function of this patient.

## 3. Results

Typical FDG- and FMZ-PET images are shown in Fig. 2. The *I/C* ratio for the cerebral glucose metabolism and FMZ binding in the striate cortex was high (cerebral glucose metabolism, >0.760; FMZ binding, >0.850) in patients 1 to 5 but low in patients 6 to 8 (Table 2-A, -B, Fig. 3-A, -B). The visual-field defects improved in patients 1 to 5 after 2 years (recovered group) but did not change in the latter 3 patients (unchanged group). The visual field has completely recovered in all recovered patients.

In the group comparison, the *I/C* ratio for the cerebral glucose metabolism in the striate cortex decreased significantly in the all patients ($P<0.0005$), i.e. in the recovered group ($P<0.005$) and the unchanged group ($P<0.05$) (Table 2-A, Fig. 3-A). The *I/C* ratio for the FMZ binding in the striate cortex decreased significantly in all the patients ($P<0.005$), i.e., in the recovered group ($P<0.05$) and unchanged group ($P<0.05$) (Table 2-B, Fig. 3-B). Further, the *I/C* ratio for the FMZ binding in the cuneus increased significantly in all the patients ($P<0.0005$), i.e., in the recovered group ($P<0.005$) and the unchanged group ($P<0.05$).

Table 2-B
Ipsilateral/contralateral (*I/C*) ratio for the $^{11}$C-flumazenil binding in each brain region in hemianopia patients

| Patient | Term (month) | Area | | | | VF |
|---|---|---|---|---|---|---|
| | | Striate cortex | Extrastriate cortex | Cuneus | Thalamus | |
| 1 | 1 | 0.914 | 0.539 | 1.116 | 1.044 | Recovered |
| 2 | 1 | 0.953 | 1.055 | 1.031 | 1.197 | Recovered |
| 3 | 2 | 0.983 | 0.472 | 1.032 | 0.938 | Recovered |
| 4 | 3 | 0.853 | 1.083 | 1.069 | 1.114 | Recovered |
| 5 | 1 | 0.935 | 0.963 | 1.057 | 0.943 | Recovered |
| 6 | 3 | 0.807 | 0.923 | 1.029 | 0.914 | Unchanged |
| 7 | 7 | 0.790 | 0.786 | 1.035 | 0.957 | Unchanged |
| 8 | 12 | 0.334 | 0.992[a] | 1.038 | 0.919 | Unchanged |
| Average for patients | | | | | | |
| | | 0.821[b] | 0.852 | 1.057[c] | 1.003 | |
| | | ±0.209 | ±0.232 | ±0.037 | ±0.105 | |
| Average for normal subjects | | | | | | |
| | | 0.997 | 1.006 | 1.000 | 0.999 | |
| | | ±0.015 | ±0.024 | ±0.003 | ±0.052 | |

VF: visual field.
[a] The extrastriate cortex of patient 8 was damaged bilaterally.
[b] Significantly lower than the value obtained for normal subjects by multiple comparisons by the Mann–Whitney *U* test ($P<0.005$).
[c] Significantly higher than the values obtained for normal subjects in multiple comparison by the Mann–Whitney *U* test ($P<0.0005$).

## 4. Discussion

Experimental research has shown that to some extent, the mature central nervous system (CNS) is capable of self-repair and reorganization following injury. The recovery of vision following stroke-induced homonymous visual field defects is well recognized, although the neurobiological mechanisms involved in recovery are controversial and poorly understood.

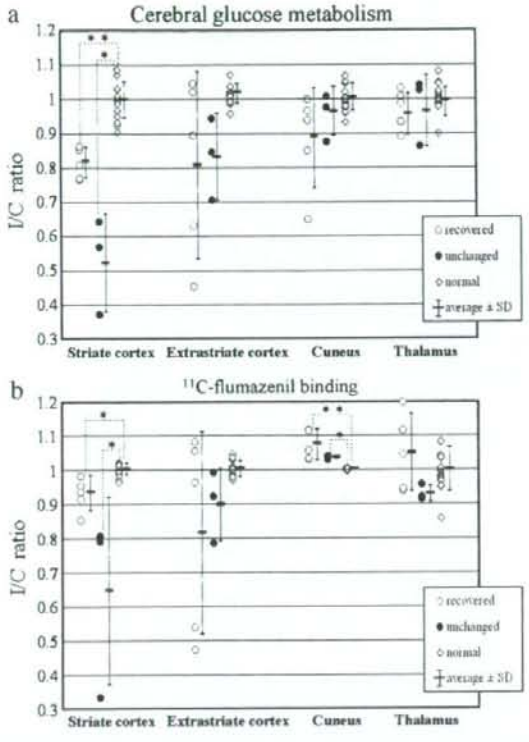


Fig. 3. A. Ipsilateral/contralateral (*I/C*) ratio for cerebral glucose metabolism in each brain region in hemianopia patients. Normal controls (gray squares, $n=15$), and 8 patients who were classified as recovered patients (circles, $n=5$) and unchanged patients (filled circles, $n=3$) are shown. As compared to the normal controls, the *I/C* ratio for cerebral glucose metabolism in the striate cortex decreased in the recovered (**; $P<0.005$) and unchanged groups (*; $P<0.05$). The *I/C* ratio for cerebral glucose metabolism in the striate cortex was more than 0.760 in 5 patients, and these patients experienced an improvement in the visual field. B. Ipsilateral/contralateral (*I/C*) ratio for the $^{11}$C-flumazenil (FMZ) binding in each brain region in hemianopia patients. Normal controls (gray squares, $n=15$) and 8 patients who were classified as recovered patients (circles, $n=5$) and unchanged patients (filled circles, $n=3$) are shown. As compared to the normal controls, the *I/C* ratio for the FMZ binding in the striate cortex decreased significantly in the recovered (*; $P<0.05$) and unchanged groups (*; $P<0.05$). The *I/C* ratio for the FMZ binding in the cuneus increased significantly in the recovered (**; $P<0.005$) and unchanged groups (*; $P<0.05$). The *I/C* ratio for the FMZ binding in the striate cortex was more than 0.850 in 5 patients, and these patients experienced an improvement in their visual field.

### *4.1. Cerebral glucose metabolism of hemianopia patients*

We observed that the *I/C* ratio for the cerebral glucose metabolism in the striate cortex decreased significantly in all the patients ($P<0.005$). Bosley et al. studied 5 hemianopia patients with ischemic lesions in order to measure the cerebral glucose metabolism by performing repeated PET scans [2]. They observed that in 2 patients, the visual field defects abated, and the PET scans revealed an improvement of glucose metabolism in the striate cortex. However, the other 3 patients did not recover vision, and the PET scans did not reveal an improvement. The cerebral glucose metabolism in the damaged area decreases immediately after the injury and then increases gradually, accompanied by recovery of function. Even if neurons in the injured area survive, glucose hypometabolism is usually observed during the early-onset stage of the disease due to the occurrence of diaschisis. For patients who show no improvement in the visual field the cerebral glucose metabolism in the damaged area does not increase. However, the glucose metabolism in the areas exhibiting diaschisis may improve at a later stage. Thus, it is difficult to accurately determine the density of the surviving neurons in the injured areas solely by the early FDG-PET findings [2].

### *4.2. $^{11}$C-flumazenil (FMZ) binding in hemianopia patients*

GABA is a major inhibitory neurotransmitter in the mammalian brain. Its postsynaptic action is largely mediated by $GABA_A$ receptors, which are integral membrane proteins that form an anion-selective channel. $GABA_A$ receptors are widely distributed in neuronal and glial cell populations in the brain; hence this receptor system is an important target for drug design. FMZ completely blocked the effects of benzodiazepines on GABA-induced currents.

We observed that the *I/C* ratio for the FMZ binding in the striate cortex was high (>0.850) in patients 1 to 5 and these patients experienced an improvement in their visual field (Table 2-A, Fig. 3-A). Diffusion-weighted MRI is commonly used for evaluating acute ischemic lesions. Heiss et al. compared the efficiency of FMZ binding and diffusion-weighted imaging (DWI) signal intensity obtained in the acute stage in predicting the prognosis of cortical infarction [9]. The cortical regions of the final infarct were accurately predicted by performing PET and DWI and were comparable; however the rate of false-positive predictions was higher with DWI. FMZ only binds to intact neurons. The use of the FMZ binding as a marker of neuronal integrity is reported to be a superior method for the early and accurate detection of cerebral damage due to ischemia [6]. However, in the acute stage, cerebral damage may progress due to continued ischemia, and the FMZ binding may gradually decrease with time. Therefore, we performed the FMZ-PET scanning at least 1 month after the organic event. The cBZR density in the lesion may reflect the number of the surviving neurons [5]. The values of the cerebral glucose metabolism

and FMZ binding are influenced by the spillover of radioactivity into neighbouring regions and the underlying tissue inhomogeneity [10], known as a 'partial volume effects', and there is a limitation measuring the values in the ROIs exactly. To understand the pathophysiological background of our results, correction of partial volume effect may be useful in the future study. We observed that recovery of the visual field can be expected among patients with a high FMZ binding in the striate cortex. The *I/C* ratio for the FMZ binding in the striate cortex and the recovery of the visual field are considered to be correlated. We propose that measurement of the cBZR density in the striate cortex of hemianopia patients relatively early during the onset of the condition is useful for the estimating the visual field recovery.

For all the patients, the *I/C* ratio for the FMZ binding in the striate cortex decreased ($P<0.005$), while that in the cuneus increased significantly ($P<0.0005$). Zepeda et al. observed that in kittens, cortical retinotopic maps are reorganized following an ischemic lesion [3]. This plasticity of the functional maps is accompanied by morphological and biochemical modifications in the area surrounding the lesion over time. Zepeda et al. also observed that the GABA content diminished and remained low from 1 to 5 weeks postlesion (wPL) and that the $GABA_A$ α1 receptor density increased from 1 to 2 wPL. These results reveal that during the reorganization of retinotopic maps following an ischemic lesion, the GABA content is reduced and the density of the postsynaptic $GABA_A$ receptor density increases due to up-regulation.

### *4.3. Prognosis of the visual field*

We observed that the *I/C* ratio for the cerebral glucose metabolism and FMZ binding in the striate cortex was high (glucose metabolism >0.760; FMZ binding >0.850) in patients 1 to 5, and that these patients experienced an improvement in their visual field. Bosley et al. studied 5 hemianopia patients, and evaluated the cerebral glucose metabolism one shortly after the ictus and once again 1 to 10 months later [2]. They reported that it is difficult to estimate the visual field prognosis solely by evaluating the glucose metabolism during the early stage. In contrast, in the present study, the cerebral glucose metabolism, which was measured more than 1 month after the onset of the condition, predicted an improvement in the visual field. Thus, evaluation of the cerebral glucose metabolism in the visual cortex more than 1 month after the onset of the condition is practically useful for estimating the prognosis of the visual field, because the predictive value of FDG-PET seems to be equivalent to that of FMZ-PET from our limited results and FDG-PET is easier to access. On the other hand, the cBZR density may reflect the number of the surviving neurons at the PET examination. Generally, acute effect of cerebral ischemic damages subside by 3 to 4 weeks after the onset, and most effective period of FMZ-PET examination for the chronic alteration may be 3 to 4 weeks after onset. Evaluating both the glucose metabolism and FMZ binding in the visual cortex in the different phases may be useful to understand the mechanisms underlying the long term recovery of hemianopia.

## 5. Conclusions

We observed that the cBZR density and affinity in the ipsilateral cuneus of hemianopia patients increased due to the presence of cerebral lesions. In hemianopia patients, measurement of both the cerebral glucose metabolism and FMZ binding in the striate cortex is useful for estimating the prognosis of the visual field.

## References

[1] Kidwell CS, Alger JR, Di Salle F, Starkman S, Villlablanca P, Bentson J, et al. Diffusion MRI in patients with transient ischemic attacks. Stroke 1999;30:1174–80.
[2] Bosley TM, Dann R, Silver FL, Alavi A, Kushner M, Chawluk JB, et al. Recovery of vision after ischemic lesions: positron emission tomography. Ann Neurol 1987;21:444–50.
[3] Zepeda A, Vaca L, Arias C, Sengpiel F. Reorganization of visual cortical maps after focal ischemic lesions. J Cereb Blood Flow Metab 2003;23:811–20.
[4] Zepeda A, Sengpiel F, Guagnelli MA, Vaca L, Arias C. Functional reorganization of visual cortical maps after focal ischemic lesions is accompanied by changes in expression of cytoskeletal proteins and NMDA and $GABA_A$ receptor subunits. J Neurosci 2004;24:1812–21.
[5] Murai H, Kiyosawa M, Suzuki Y, Mizoguchi S, Ishii K, Ishiwata K, et al. A case of multiple sclerosis with homonymous hemianopia examined by positron emission tomography. Jpn J Ophthalmol 2004;48:591–3.
[6] Heiss WD, Kracht L, Grond M, Rudolf J, Bauer B, Wienhard K, et al. Early [$^{11}$C] flumazenil/$H_2O$ positron emission tomography predicts irreversible ischemic cortical damage in stroke patients receiving acute thrombolytic therapy. Stroke 2000;31:366–9.
[7] Mishina M, Senda M, Kimura Y, Toyama H, Ishiwata K, Ohyama M, et al. Intrasubject correlation between static scan and distribution volume images for [$^{11}$C] flumazenil PET. Ann Nucl Med 2000;14: 193–8.
[8] Ardekani BA, Braun M. A fully automatic multimodality image registration algorithm. J Comput Assist Tomogr 1995;19:615–23.
[9] Heiss WD, Sobesky J, Smekal U, Kracht LW, Lehnhardt FG, Thiel A, et al. Probability of cortical infarction predicted by flumazenil binding and diffusion-weighted imaging signal intensity: a comparative positron emission tomography/magnetic resonance imaging study in early ischemic stroke. Stroke 2004;35:1892–8.
[10] Soret M, Bacharach SL, Buvat I. Partial-volume effect in PET tumor imaging. J Nucl Med 2007;48:932–45.

# Presynaptic and postsynaptic nigrostriatal dopaminergic functions in multiple system atrophy

Masaya Hashimoto[a,c], Keiichi Kawasaki[a], Masahiko Suzuki[a,c], Kazuko Mitani[a,d], Shigeo Murayama[b], Masahiro Mishina[a,e], Keiichi Oda[a], Yuichi Kimura[a], Kiichi Ishiwata[a], Kenji Ishii[a] and Kiyoharu Inoue[c]

[a]Positron Medical Center, [b]Department of Neuropathology, Tokyo Metropolitan Institute of Gerontology, [c]Department of Neurology, Jikei University School of Medicine, [d]Department of Neurology, Tokyo Metropolitan Geriatric Hospital, Tokyo and [e]Neurological Institute, Nippon Medical School Chiba Hokusoh Hospital, Chiba, Japan

Correspondence to Kenji Ishii, Positron Medical Center, Tokyo Metropolitan Institute of Gerontology, 1-1 Naka-cho, Itabashi-ku, Tokyo 173-0022, Japan
Tel: +81 3 3964 3241 EX3503; fax: +81 3 3964 2188; e-mail: ishii@pet.tmig.or.jp

Received 7 September 2007; accepted 30 October 2007

A simultaneous evaluation of presynaptic and postsynaptic dopaminergic positron emission tomography markers, the dopamine transporters and the dopamine $D_2$-like receptors, was performed in eight patients with parkinsonian phenotype of multiple system atrophy. Both presynaptic and postsynaptic markers were revealed to have declined in such a manner that they kept strong positive correlation throughout the striatum of all patients, suggesting that the degeneration process in the striatum may involve the entire structure of the dopaminergic synapse. In two L-3,4,dihydroxyphenyl-alanine-responsive cases, the balance of decline in two markers was relatively shifted to presynaptic dominant side. Correlative positron emission tomography study of presynaptic and postsynaptic dopaminergic function may be useful for the diagnosis of multiple system atrophy and to understand the mechanisms of its temporal L-3,4,dihydroxyphenyl-alanine responsiveness. *NeuroReport* 19:145–150 © 2008 Wolters Kluwer Health | Lippincott Williams & Wilkins.

**Keywords**: dopamine receptor, dopamine transporter, L-3,4,dihydroxyphenyl-alanine responsiveness, multiple system atrophy, Parkinson, positron emission tomography

## Introduction

In patients with the parkinsonian phenotype of multiple system atrophy (MSA-P), a pathological abnormality is observed mainly in the substantia nigra (SN), striatum, ceruleus nucleus, pontine nuclei, inferior olivary nucleus, cerebellum, and spinal cord. The impairment is particularly severe in the SN and striatum [1], and neuronal loss and gliosis are the features of the pathology [2]. Neuroimaging studies using positron emission tomography (PET) [3] and single photon emission computed tomography techniques [4] have reported reduced glucose metabolism in the striatum and declined nigrostriatal dopaminergic neural transmission function in both the presynaptic and postsynaptic sites. No pathological or neuroimaging studies, however, have examined the relationship between the degeneration/dysfunction of nigrostriatal presynaptic and postsynaptic dopaminergic systems. It is well known that responses to L-3,4,dihydroxyphenyl-alanine (L-DOPA) are generally poor in MSA [1], and this is ascribable to the fact that the pathology of MSA involves not only SN but also the striatum where the dopamine receptors exist. A transient effect, however, is occasionally noted in the early stages in certain cases. Wenning *et al.* [5] proposed a hypothesis based on the pathological finding of a dissociation between the SN and striatal degeneration that may account for such L-DOPA responsiveness. No pathological or neuroimaging evidence that directly demonstrated the dissociation in such cases, however, has been found.

We simultaneously measured the presynaptic and postsynaptic nigrostriatal dopaminergic functions using PET in MSA-P patients, including L-DOPA-responsive cases, and the regional correlation of two parameters was analyzed in the striatum to examine the characteristics of the disease and the mechanisms of L-DOPA responsiveness.

## Methods

This study was approved by the Ethical Committee of Tokyo Metropolitan Institute of Gerontology. The objective and effect of the PET examination on the human body were adequately explained to all participants, and written informed consent was obtained.

### Participants

We studied eight patients (68.9±7.4 years old) clinically diagnosed as MSA-P according to the consensus criteria established by Gilman *et al.* [6] (Table 1). The MSA-P patients underwent PET examination following a 15-h deprivation of antiparkinsonian drugs. The primary symptom observed in all the patients was parkinsonism; further, during the course of the disease, parkinsonism was noted to be the cardinal symptom. Magnetic resonance imaging (MRI) examination was also performed. The characteristics of the patients are presented in Table 1. Among the eight cases of MSA-P, cases 1 and 2 apparently responded to L-DOPA at the time of the PET study, and the improvement

**Table 1** Clinical features of the eight patients with the parkinsonian phenotype of multiple system atrophy

| Patient no./age (years)/sex | Hoehn and Yahr stage | Disease duration (years) | Autonomic dysfunction | Cerebellar dysfunction | Pyramidal sign | MRI findings | L-DOPA response |
|---|---|---|---|---|---|---|---|
| 1/79/Female | III | 1 | + | + | + | Put | + |
| 2/73/Female | III | 1 | + | + | + | Put | + |
| 3/66/Female | I | 2 | + | + | + | No findings | – |
| 4/61/Female | IV | 2 | + | + | + | cbll/put | – |
| 5/72/Male | V | 3 | + | – | + | Put | – |
| 6/56/Male | IV | 4 | + | + | + | Pons/cbll/put | – |
| 7/73/Female | III | 6 | + | + | + | Pons/cbll/put | – |
| 8/71/Female | V | 9 | + | – | + | Put | – |

Signal change in the pons/middle cerebellar peduncles includes pontine/cerebellar atrophy (pons/cbll); Slit-like signal change at the posterolateral putaminal margin includes putaminal atrophy (put). L-DOPA, L-3,4,dihydroxyphenyl-alanine.

in the symptoms of parkinsonism due to L-DOPA was confirmed by neurologists.

The healthy control group consisted of eight participants (five men and three women, 62.3±6.9 years old) that did not have a past medical history of neurological and psychiatric disorders. They were diagnosed as normal after physical and neurological examinations, screening MRI scans, and Mini-Mental Scale Evaluation (>28). They had not taken any neuroleptic drugs and were not addicted to alcohol; no history of any other substance abuse was present.

### Positron emission tomography scans

$^{11}$C-labeled 2β-carbomethoxy-3β-(4-fluorophenyl)-tropane ([$^{11}$C]CFT) as a marker of presynaptic dopaminergic function for dopamine transporters and $^{11}$C-labeled raclopride ([$^{11}$C]RAC) as a marker of postsynaptic dopaminergic function for dopamine $D_2$-like receptors were used as tracers for PET [7,8]. The methods used for the preparation of the radiopharmaceuticals were as described previously [9,10].

All the participants underwent the two PET studies on the same day with a 3–4-h interval. PET images were acquired in three-dimensional mode using the SET-2400W (Shimadzu, Kyoto, Japan) scanner [11] at the Positron Medical Center, Tokyo Metropolitan Institute of Gerontology. The acquired PET images were 128 × 128 × 50 in matrix size with a 2 × 2 × 3.125-mm voxel size. In PET acquisition, 300 MBq each of [$^{11}$C]CFT and [$^{11}$C]RAC were administered by an intravenous bolus injection, and all participants rested in a supine position with their eyes open during the test. The specific activity and the amount of cold material injected were 5.4–47 MBq/nM and 1.2–8.6 nM, respectively, for [$^{11}$C]CFT and 10–130 MBq/nM and 0.42–3.1 nM, respectively, for [$^{11}$C]RAC. For three of the eight healthy control participants, a dynamic scan was performed for 90 min for the [$^{11}$C]CFT study in the morning and for 60 min for the [$^{11}$C]RAC study in the afternoon to estimate the binding potentials. To measure the uptakes of these two tracers, for the five healthy participants and all the patients, a static scan was performed 75–90 min after the injection of the [$^{11}$C]CFT and 40–55 min after the injection of [$^{11}$C]RAC, respectively. The attenuation was corrected by a transmission scan using a $^{68}$Ga/$^{68}$Ge source.

### Data analysis

The two PET images of the [$^{11}$C]CFT and [$^{11}$C]RAC examinations obtained from the same participant were coregistered using an automated image registration program [12]. The images were processed further using Dr View software (AJS, Tokyo, Japan) on Linux workstations. Next, the images were resliced in the transaxial direction parallel to the anterior–posterior intercommissural (AC-PC) line, and the regions of interest (ROIs) were placed on the three subregions of the striatum – the bilateral caudate nuclei, anterior putamen, and posterior putamen – in two slices, that is, the AC-PC plane and 3.1 mm above the AC-PC line. ROIs of the striatum consisted of circles of 8-mm diameter. On each side of each slice, we set one ROI in the caudate and two ROIs each in the anterior and posterior putamen. The reference regions of the occipital lobe were placed in four slices in a range of 12.5–21.9 mm above the AC-PC plane. The reference region of the occipital lobe consisted of circles of 10-mm diameter, and we set four such circles on each side of each slice.

First, for dynamic scan data, the binding potential of the tracer in the bilateral caudate nuclei, anterior putamen, and posterior putamen of three healthy participants was estimated by a simplified reference region model [13] using the occipital lobe as a reference. Second, for static imaging, the uptake ratio index (URI) was calculated for all participants by the following formula:

$$\mathrm{URI} = \left(\mathrm{Activity}_{\mathrm{Striatum\ subregion}} - \mathrm{Activity}_{\mathrm{Occipital\ lobe}}\right) / \mathrm{Activity}_{\mathrm{Occipital\ lobe}}$$

URI was also calculated for the dynamic scan in the three healthy control participants using the data obtained from an equivalent time-frame. The URI in each ROI was compared between MSA-P patients and control participants with the Mann–Whitney *U*-test with Bonferroni's correction for multiple comparisons.

Next, we examined the correlation between the binding potential and the URI.

## Results

For each tracer, the URIs of the striatal subregions in the static image were linearly correlated with the binding potentials in the dynamic scan ($r^2$=0.92, $P$<0.0001 for [$^{11}$C]CFT and $r^2$=0.93, $P$<0.0001 for [$^{11}$C]RAC). Therefore, we adopt the URI in reference to the occipital cortex for the further analysis.

Figure 1 demonstrates the representative PET images of a normal participant and an MSA-P patient. In the MSA-P patient, the URIs of both [$^{11}$C]CFT and [$^{11}$C]RAC declined in the striatum compared with the normal participant (Fig. 1).

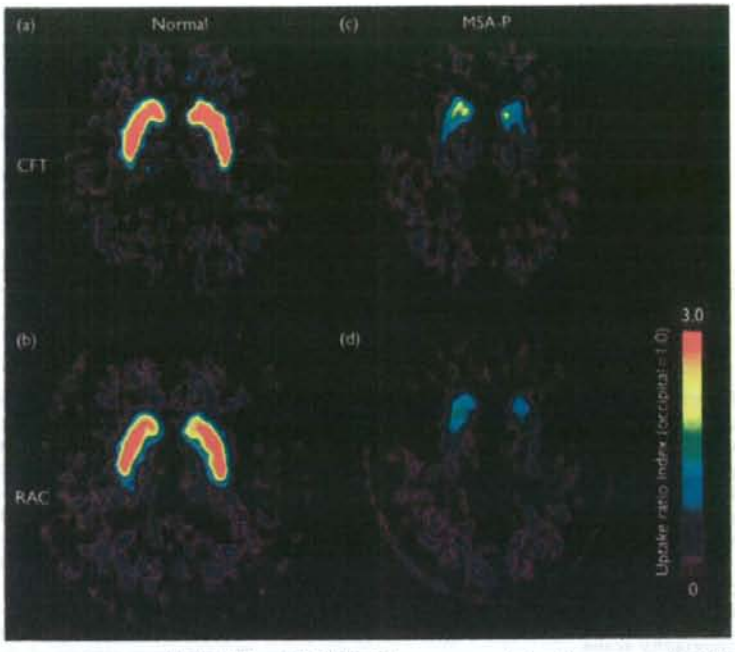


**Fig. 1** Positron emission tomography images. (a) [$^{11}$C]CFT and (b) [$^{11}$C]RAC images were obtained from a normal participant, and (c) [$^{11}$C]CFT and (d) [$^{11}$C]RAC images were obtained from an MSA-P patient. All the images were normalized to the occipital lobe activity and obtained in a +3.1-mm plane from the anterior–posterior intercommissural line. [$^{11}$C]CFT, $^{11}$C-labeled 2β-carbomethoxy-3β-(4-fluorophenyl)-tropane; [$^{11}$C]RAC, $^{11}$C-labeled raclopride; MSA-P, phenotype of multiple system atrophy.

**Table 2** The uptake ratio index of [$^{11}$C]CFT and [$^{11}$C]RAC in the subregions of the striatum

| | Normal participants ($n$=8) | MSA-P patients ($n$=8) | Percentage of control |
|---|---|---|---|
| Caudate | | | |
| [$^{11}$C]CFT | 3.70±0.55 | 2.49±0.41* | 67.3 |
| [$^{11}$C]RAC | 3.46±0.40 | 2.63±0.31* | 76.0 |
| Anterior putamen | | | |
| [$^{11}$C]CFT | 4.04±0.45 | 1.97±0.45* | 48.8 |
| [$^{11}$C]RAC | 3.97±0.31 | 2.46±0.46* | 62.0 |
| Posterior putamen | | | |
| [$^{11}$C]CFT | 3.82±0.47 | 1.58±0.42* | 41.4 |
| [$^{11}$C]RAC | 3.90±0.32 | 2.07±0.67* | 53.1 |

*$P$<0.05 as compared with normal controls (Mann–Whitney $U$-test with Bonferroni's multiple comparison correction).
[$^{11}$C]CFT, $^{11}$C-labeled 2β-carbomethoxy-3β-(4-fluorophenyl)-tropane; [$^{11}$C]RAC, $^{11}$C-labeled raclopride; MSA-P, phenotype of multiple system atrophy.

The results of ROI measurement are summarized in Table 2. In the MSA-P group, the URIs of both [$^{11}$C]CFT and [$^{11}$C]RAC significantly decreased in all the subdivisions of the striatum ($P$<0.05) in comparison with the control group, and the decrease was most prominent in the posterior putamen and relatively smaller in the caudate nuclei.

Scatter plots of the entire uptake data in individual participants for each of the three regions are shown in Fig. 2a–c and those for all areas are shown in Fig. 2d. A strong positive correlation was noted between the URIs of [$^{11}$C]CFT and [$^{11}$C]RAC in the MSA-P group. That is, the impairment of presynaptic and postsynaptic nigrostriatal dopaminergic function was observed in associative degree in all the subregions of the striatum.

Two patients apparently responded to the L-DOPA administration at the time of PET studies. Figure 2 indicates that the decrease in the [$^{11}$C]RAC uptake was relatively lesser in comparison with that in the [$^{11}$C]CFT uptake in the L-DOPA-responsive cases.

## Discussion

In earlier studies, the cerebellum has been widely used as a reference region to estimate the availability of dopamine transporters using [$^{11}$C]CFT [14,15] and dopamine $D_2$-like receptors using [$^{11}$C]RAC [16]. We, however, selected the occipital cortex as a reference region in this study. Neuropharmacological evidence has revealed that the densities of both the dopamine transporters and dopamine $D_2$-like receptors in the human occipital cortex are negligible as in the case of the cerebellum [17]. Furthermore, the cerebellum is often involved in the pathological processes in MSA-P, whereas the occipital lobe is less likely to be affected. The selection of the occipital region as a reference would be useful for PET analysis of MSA. In contrast, the measured values of the striatum might have been affected by the atrophy. The correlation of two PET measures on the same regions, however, are robust because they are evaluated with common ROIs to cancel out the spatial effect.

Using [$^{11}$C]CFT and [$^{11}$C]RAC, we simultaneously measured presynaptic and postsynaptic nigrostriatal dopaminergic

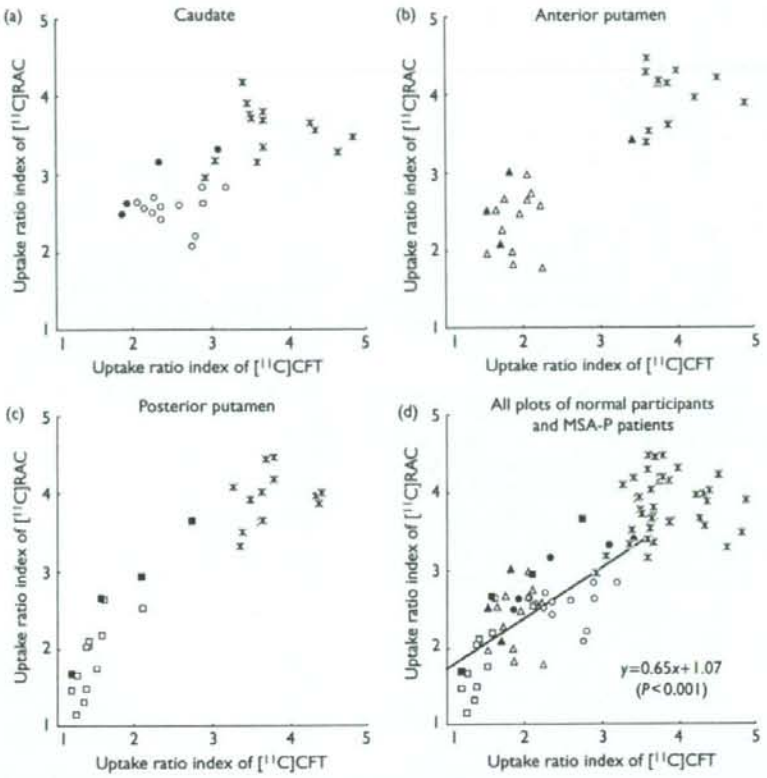


**Fig. 2** The correlation between the uptake ratio index (URI) of [$^{11}$C]CFT and that of [$^{11}$C]RAC in the caudate nuclei (a), anterior putamen (b), posterior putamen (c), and all these areas (d) of all participants including MSA-P patients ($n$=8) and normal participants ($n$=8). The approximate lines for all the plots of the MSA-P group are shown in (d). Asterisk (*), normal participants; open circles (○), the caudate nuclei in MSA-P patients; open triangles (Δ), the anterior putamen in MSA-P patients; open squares (□), the posterior putamen in MSA-P patients; and solid markers (●), MSA-P patients exhibiting L-DOPA responsiveness. [$^{11}$C]CFT, $^{11}$C-labeled 2β-carbomethoxy-3β-(4-fluorophenyl)-tropane; [$^{11}$C]RAC, $^{11}$C-labeled raclopride; L-DOPA, L-3,4,dihydroxyphenyl-alanine; MSA-P, phenotype of multiple system atrophy.

functions and observed that both functions were significantly impaired in all eight patients with MSA-P compared with the normal group.

The functional impairment in the striatum was more noticeable in the putamen, particularly in its posterior part, than in the caudate nuclei. The most prominent result of our study was that a strong positive correlation was noted between presynaptic and postsynaptic functional impairments in the MSA-P group throughout the striatum regardless of the severity of the impairments. In Parkinson's disease (PD), presynaptic and postsynaptic functional impairments were reported to be negatively correlated in the putamen by PET using [$^{11}$C]CFT and [$^{11}$C]SCH 23390 (dopamine $D_1$-like receptor probe), reflecting severe impairment in the presynaptic marker with an upregulation of the postsynaptic function [18]. The differential diagnosis between MSA-P and PD in clinical situations is at times difficult. The patterns of presynaptic and postsynaptic functional impairments, however, demonstrated by PET contrasted between MSA-P and PD, and therefore the two disorders can be clearly differentiated with combined presynaptic and postsynaptic dopaminergic PET examinations.

Ghaemi *et al.* [3] applied PET using [$^{18}$F]FDOPA and [$^{11}$C]RAC to MSA-P patients and discovered that both presynaptic and postsynaptic dopaminergic functions were reduced in the nigrostriatal dopaminergic system. They did not, however, provide information about whether the impairments in the presynaptic and postsynaptic dopaminergic function were correlated in each patient. Our study is the first to demonstrate a positive correlation between the presynaptic and postsynaptic dopaminergic function with respect to the local subdivisions of the striatum and the disease duration.

What is the pathological background of the strong correlation of presynaptic and postsynaptic markers measured by PET? Pathologically, neuronal loss and gliosis are the primary forms of impairment in MSA [2]. The neuronal loss tends to be severe in both SN and striatum; however, it is not always to the same extent [1], and there has been no report regarding the correlation of pathological findings such as glial cytoplasmic inclusion [19] and α-synuclein [20,21] between SN and striatum. If the PET markers for presynaptic and postsynaptic dopaminergic function directly reflect the degree of degeneration in SN and striatum

independently, as in PD [15,22], the combination in the degree of presynaptic and postsynaptic functional impairment could be variable. The presence of a strong positive correlation between the presynaptic and postsynaptic dopaminergic functions measured by PET within patients and across patients suggests that these impairments in MSA-P are the result of the destruction of the entire synaptic structure in the striatum. Pathologically, the putamen is one of the areas with the most severe neuronal loss in MSA-P [2]. We consider that the presynaptic marker represents the degree of degeneration of the SN only if the striatum involvement is lesser than that of SN; however, once the severe destruction of striatum occurs, the presynaptic marker no longer represents the degree of SN degeneration because it is masked by the destruction of the entire structure of the synapse.

Parkinsonism in MSA is treated with L-DOPA, dopamine agonists, and anticholinergic agents; however, only a mild effect is noted in a minor population in the early stage, and the responsiveness to L-DOPA gradually disappears. Generally, responses to L-DOPA are poor in cases of MSA-P [1]. In a previous report, L-DOPA was effective in the early stage in approximately 1/3 of the MSA cases [23]. We examined two early MSA-P cases responsive to L-DOPA. In these cases, the presynaptic dopaminergic function was markedly reduced; however, the reduction in the postsynaptic dopaminergic function was relatively less severe compared with that in the cases not responsive to L-DOPA; moreover, this trend was more prominent in the striatum on the contralateral side in which L-DOPA alleviated the symptoms of parkinsonism. Churchyard *et al.* [24] suggested that the ineffectiveness of L-DOPA on parkinsonism in MSA is related to the dominance of neuronal loss, gliosis, and the reduction in postsynaptic dopamine $D_2$ receptors in the posterior putamen. Wenning *et al.* [5] reported that L-DOPA was highly effective in the cases in which the putamen was relatively conserved compared with the degree of nigral neuronal loss, and the effect of L-DOPA was negatively correlated with the degree of nigral degeneration, suggesting that nigral degeneration precedes striatal degeneration [1]. Whether nigral degeneration preceded striatal degeneration was not clear in our study; however, postsynaptic dopaminergic function was relatively retained in our L-DOPA-responsive cases. We consider that the degree of conservation of postsynaptic dopaminergic function is related to the effectiveness of L-DOPA in MSA-P and that a trend of dissociation of presynaptic and postsynaptic markers can be detected by PET. Further studies are necessary to increase the number of the participants and to follow up the L-DOPA-responsive cases using PET and clinical course observations.

## Conclusion

We have established the presence of a strong positive correlation between the reductions in nigrostriatal presynaptic and postsynaptic dopaminergic functions and L-DOPA-responsive cases in which the degrees of presynaptic and postsynaptic functional impairments are dissociated in some manner.

The elucidation of the patterns and processes of presynaptic and postsynaptic functional impairments may provide a clue to understanding the development and advancement mechanisms of the disease and will aid in a more reliable early clinical diagnosis and prediction of drug effects.

## References


1. Wenning GK, Ben-Shlomo Y, Magalhaes M, Daniel SE, Quinn NP. Clinicopathological study of 35 cases of multiple system atrophy. *J Neurol Neurosurg Psychiatry* 1995; **58**:160–166.
2. James SL, Nigel L. Disorders of movement and system degeneration. In: David IG, Peter LL, editors. *Greenfield's Neuropathology*. 7th ed. Vol. 2. London: Arnold; 2002. pp. 325–430.
3. Ghaemi M, Hilker R, Rudolf J, Sobesky J, Heiss WD. Differentiating multiple system atrophy from Parkinson's disease: contribution of striatal and midbrain MRI volumetry and multi-tracer PET imaging. *J Neurol Neurosurg Psychiatry* 2002; **73**:517–523.
4. Van Royen E, Verhoeff NP, Speelman JD, Wolters EC, Kuiper MA, Janssen AG. Multiple system atrophy and progressive supranuclear palsy. Diminished striatal $D_2$ dopamine receptor activity demonstrated by $^{123}$I-IBZM single photon emission computed tomography. *Arch Neurol* 1993; **50**:513–516.
5. Wenning GK, Quinn N, Magalhaes M, Mathias C, Daniel SE. 'Minimal change' multiple system atrophy. *Mov Disord* 1994; **9**:161–166.
6. Gilman S, Low P, Quinn N, Albanese A, Ben-Shlomo Y, Fowler C, *et al.* Consensus statement on the diagnosis of multiple system atrophy. American Autonomic Society and American Academy of Neurology. *Clin Auton Res* 1998; **8**:359–362.
7. Volkow ND, Fowler JS, Gatley SJ, Logan J, Wang GJ, Ding YS, *et al.* PET evaluation of the dopamine system of human brain. *J Nucl Med* 1996; **37**:1242–1256.
8. Booij J, Tissingh G, Winogrodzka A, van Royen EA. Imaging of the dopaminergic neurotransmission system using single-photon emission tomography and positron emission tomography in patients with parkinsonism. *Eur J Nucl Med* 1999; **26**:171–182.
9. Kawamura K, Oda K, Ishiwata K. Age-related changes of the [$^{11}$C]CFT binding to the striatal dopamine transporters in the Fischer 344 rats: a PET study. *Ann Nucl Med* 2003; **17**:249–253.
10. Langer O, Någren K, Dolle F, Lundkvist C, Sandell J, Swahn CG, *et al.* Precursor synthesis and radiolabelling of the dopamine $D_2$ receptor ligand [$^{11}$C]raclopride from [$^{11}$C]methyl triflate. *J Labelled Comp Radiopharm* 1999; **42**:1183–1193.
11. Fujiwara T, Watanuki S, Yamamoto S, Miyake M, Seo S, Itoh M, *et al.* Performance evaluation of a large axial field-of-view PET scanner: SET-2400W. *Ann Nucl Med* 1997; **11**:307–313.
12. Ardekani BA, Braun M, Hutton BF, Kanno I, Iida H. A fully automatic multimodality image registration algorithm. *J Comput Assist Tomogr* 1995; **19**:615–623.
13. Gunn RN, Lammertsma AA, Hume SP, Cunningham VJ. Parametric imaging of ligand-receptor binding in PET using a simplified reference region model. *NeuroImage* 1997; **6**:279–287.
14. Wong DF, Yung B, Dannals RF, Shaya EK, Ravert HT, Chen CA, *et al.* In vivo imaging of baboon and human dopamine transporters by positron emission tomography using [$^{11}$C]WIN 35428. *Synapse* 1993; **15**:130–142.
15. Frost JJ, Rosier AJ, Reich SG, Smith JS, Ehlers MD, Snyder SH, *et al.* Positron emission tomographic imaging of the dopamine transporter with $^{11}$C-WIN 35,428 reveals marked declines in mild Parkinson's disease. *Ann Neurol* 1993; **34**:423–431.
16. Antonini A, Leenders KL, Reist H, Thomann R, Beer HF, Locher J. Effect of age on $D_2$ dopamine receptors in normal human brain measured by positron emission tomography and $^{11}$C-raclopride. *Arch Neurol* 1993; **50**:474–480.
17. Mozley PD, Stubbs JB, Kung HF, Selikson MH, Stabin MG, Alavi A. Biodistribution and dosimetry of iodine-123-IBF: a potent radiolig and for imaging the D2 dopamine receptor. *J Nucl Med* 1993; **34**: 1910–1917.
18. Ouchi Y, Kanno T, Okada H, Yoshikawa E, Futatsubashi M, Nobezawa S, *et al.* Presynaptic and postsynaptic dopaminergic binding densities in the nigrostriatal and mesocortical systems in early Parkinson's disease: a double-tracer positron emission tomography study. *Ann Neurol* 1999; **46**:723–731.
19. Papp MI, Kahn JE, Lantos PL. Glial cytoplasmic inclusions in the CNS of patients with multiple system atrophy (striatonigral degeneration,